TECHNISCHE
UNIVERSITÄT
WIEN
Vienna University of Technology

Master Thesis

Carrier gas enhanced focused electron beam induced deposition of cobalt for 3D nanomagnet logic devices

Institute of Solid State Electronics

Vienna University of Technology

under supervision of

O. Univ. Prof. Dr. Emmerich Bertagnolli

Ass. Prof. Dr. Heinz Wanzenböck

by

Stefan Wachter

Matr.Nr. 0725606

Acknowledgement

This thesis marks the end of my time as a student at the Vienna University of Technology and a major period of my life. I would like to use this page to thank several people, without whom the past several years at the university would not have been the same.

O.Univ.Prof. Dr. Emmerich Bertagnolli for giving me the opportunity to work on my thesis at the institute for solid state electronics.

Ass.Prof. Dr. Heinz Wanzenböck for co-supervising my thesis, providing me with many great opportunities and experiences I did not expect to have during the past months and for making me a valued member of his working group.

Dr. Marco Gavagnin with whom I had the pleasure to work with for the majority of the time spent on my thesis and share many discussions, scientific or not. I would also like to thank him for the patience required to teach an electrical engineer about chemistry.

My friends - Thomas, Kaufi, Schirmer and Luigi for a lot of high quality jokes, riddles and fun times, as well as making the whole trip a team effort.

The final words of acknowledgement are dedicated to my parents and my girlfriend Silke for providing me with all the encouragement and support one could wish for.

Abstract

The deposition and structuring of materials on the nanoscale is among the most important technologies in existence today. One method of creating nanostructures in a maskless and direct-write way is focused electron beam induced deposition. This work describes the application of a novel gas injection system for this method allowing for the use of a carrier gas in order to increase and better control the flux of a low vapor pressure precursor into the vacuum chamber. Several carrier gases, namely nitrogen, hydrogen and oxygen, were investigated with regard to the deposition rate and chemical composition of the resulting deposits, confirming the feasibility of the use of a carrier gas in focused electron beam deposition. The results obtained in this work pave the way for further research in a second area this work investigates – three dimensional nanomagnet logic structures. This technology can be used to magnetically store and process information with potentially far lower energy demands than CMOS is able to and is therefore a potential beyond-CMOS candidate. Using focused electron beam induced deposition quick development and fabrication of several three dimensional gate-designs was performed resulting in a working magnetic majority gate.

Table of contents

Acknowledgement 3

Abstract 5

0) Table of contents 6

1) Introduction 9

2) Theoretical aspects 12

2.1) Nanomagnet Logic 12

2.1.1) Motivation 12

2.1.2) Basic Principles of NML 13

2.2) Focused Electron Beam Induced Deposition 19

2.2.1) Motivation 19

2.2.2) Basic Principles of FEBID 20

2.3) Characterization Methods 23

2.3.1) SEM - EDX 23

2.3.2) Atomic Force Microscopy / Magnetic Force Microscopy 27

3) Experimental 34

3.1) Fabrication 34

3.1.1) LEO 1530VP 34

3.1.2) The Gas Injection System 35

3.1.2) Pattern Generator 38

3.1.3) Substrate 40

3.1.4) Design of the structures 41

3.1.5 Deposition procedure 44

3.2) Characterization 45

3.2.1) Energy-dispersive X-ray spectroscopy 45
3.2.2) AFM / MFM 46
4) Carrier Gas Enhanced FEBID 49
4.1) Motivation and Overview 49
4.2) Methods and Experimental Details 50
4.3) Results and Discussion 51
4.3.1) Nitrogen as a Carrier Gas 51
4.3.2) Hydrogen as a Carrier Gas 59
4.3.3) Oxygen as a Carrier Gas 62
5) Nanomagnet Logic (NML) 65
5.1) NML using three dimensional Fe structures by FEBID 65
5.1.1) Motivation 65
5.1.2) Designs 65
5.1.3) Experimental 67
5.2) Results and Discussion 67
6) Conclusion and Outlook 73
7) Appendices 75
7.1 List of Abbreviations 75
7.2 List of Figures 77
7.3 Bibliography 79

1) Introduction

A lot of attention has been directed towards ferromagnetic nanostructures in the past years. The usual approach for fabrication of these structures is a combination of lithographic steps, blanket chemical vapor deposition and a subsequent lift-off process [1,2]. This work investigates focused electron beam induced deposition (FEBID), an alternative technique for the nanoscale fabrication of such nanostructures, and one application thereof, nanomagnet logic (NML). In order to achieve deposition, the focused electron beam of a scanning electron microscope (SEM) locally supplies the energy needed to activate the precursor and induce a locally confined chemical vapor deposition process. FEBID, as a mask- and resist-less nanofabrication technique allows for the fabrication of planar and three dimensional structures in one single process step, which enables high flexibility in the (three dimensional) design of deposited objects, while avoiding complex and time consuming multi step lithography processes. This makes FEBID an excellent candidate for research and prototyping application in many areas out of which the focus of this work lies on NML [3–6].

NML is a beyond CMOS technology for storage and processing of digital information [7]. One of the problems CMOS technology is facing is the increasing power density [8] with shrinking transistor sizes approaching values comparable to rocket nozzles. By no longer relying on the storage and movement of electric charges for data processing and storage but on the non-volatile orientation of the magnetic moment of ferromagnetic nanostructures this issue can potentially be avoided by drastically reducing the power per switching event in digital circuitry [9]. NML gates consist of magnetic nanostructures which are engineered to have high shape anisotropy. This causes them to exhibit biaxial behavior, which is used for the transport, storage and processing of digital information by magnetic coupling between individual nanostructures. Several designs of 3 dimensional logic gates where fabricated from Fe and investigated by magnetic force microscopy (MFM). However it is expected that structures comprised of Co or a mixture of Co and Fe would display better coupling between these nanostructures, due to the higher coercivity of Co compared to Fe. A controlled deposition of Co however is not as straightforward as with Fe,

mainly because of the different physical properties of the precursor material, e.g. the very different vapor pressure.

It is due to this that while a large part of the work focuses on the deposition of Co, the fabrication of NML gates and structures was performed solely using Fe. This allows the focus of the work on NML to be on the actual design of the structures instead of the control of the deposition parameters.

A crucial property of the nanostructures employed in NML aside from their shape is of course their metal content, which greatly influences their magnetic behavior. Generally, a high metal content is desirable. Deposition of highly pure magnetic materials based on Fe and Co by FEBID based on carbonyl (CO)-based precursors has already been demonstrated by several works [3,6]. The choice of these chemicals stems from their high volatility and relatively 'clean' decomposition path [10]. In order to achieve clean and reproducible deposition the conditions under which this deposition is performed must be tightly controlled. The amount of precursor supplied, as well as focused electron beam (FEB) current are the two main parameters, aside from chamber contaminations, that influence the deposited structures. While the FEB current can be reliably controlled by the aperture of the SEM, precursor flux is harder to control [11]. Precursors with a comparably high vapor pressure like iron-pentacarbonyl are usually flux-controlled by simply constricting the flow with a needle valve or a mass flow controller (MFC). The precursor available for deposition of cobalt (Co_2CO_8) however has a relatively low vapor pressure where such a strategy is not feasible. The commonly employed strategy to increase evaporation of low vapor pressure materials is heating [5,12]. This however causes significant problems, since any temperature gradient along the delivery system can cause re-condensation or premature decomposition and deposition of precursor molecules in the gas injection system (GIS) itself instead of the target substrate.

In order to be able to control the flux of Co precursor, a gas injection system (GIS) was built, which allows enhancing the injection of precursor using a controllable amount of carrier gas. This carrier gas is expected to increase the flux of the precursor by keeping the atmosphere in the reservoir from saturating with gaseous precursor by removing them using the kinetic energy from the carrier gas molecules. Aside from this enhanced and controllable delivery of precursor to the chamber,

chemical reactions between the carrier gas and the precursor or fragments thereof might also influence the depositions. To study these effects nitrogen, oxygen and hydrogen where chosen as a carrier gas. Nitrogen as an inert gas was chosen to avoid any chemical reactions in order to separately study the kinetic effects on the precursor. Oxygen and hydrogen on the other hand where chosen for their oxidizing and reducing properties, respectively, which could lead to a cleaner decomposition path of the precursor.

The work on the deposition of cobalt may be seen as a stepping stone towards future work on the fabrication of NML gates from cobalt or even of iron-cobalt composites or alloys.

2) Theoretical aspects

In this chapter the main concepts and tools of this work are explained. It should present an overview of the techniques used and enable a reader who is not familiar with the subject to understand the reasoning behind their use and the interpretation of the results they yield.

2.1) Nanomagnet Logic

2.1.1) Motivation

The ever increasing demand for processing power and data storage has lead to a tremendously fast shrinking of structure sizes in the semiconductor industry. While 10 years ago, the feature manufacturing process of mainstream CPUs was typically at 100-160nm, todays[1] commercially available CPUs are manufactured at a feature size of 22 nm. Aside from several major electronic complications caused by this shrinkage, one of the main problems to be solved for each new generation is the dissipation of excess heat. The race to increase processor frequencies has driven the power density in usual desktop CPUs to 100 W/cm^2 (see **Figure 1**), which is about an order of magnitude higher than an average hot plate. Tough this is still three orders of magnitude worse than the theoretical limit, this has become a major problem for the electronics industry [8,13]. While improved cooling and thermal conductivity along with improved design of the integrated electronics leading to more efficient computing has enabled continuous progress in the semiconductor industry, a new technology as a possible successor to the current CMOS architecture seems to be necessary in the foreseeable future. One of those so called beyond-CMOS technologies addressed in the International Technology Roadmap for Semiconductors (ITRS) is Nanomagnet Logic. According to the ITRS, NML can potentially solve the problem of heat dissipation [14] by offering a non volatile technology that is not based on the movement of electrical charge, thereby avoiding major problems like leakage current and switching transients.

---

[1] June 2014

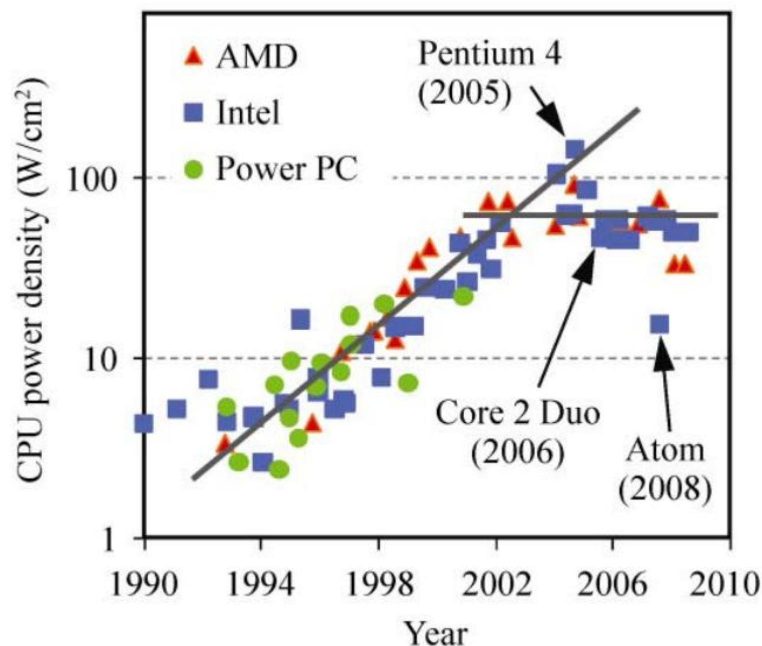

Figure 1 *– Heat density trend of common consumer desktop CPUs (taken from [8]).*

2.1.2) Basic Principles of NML

As briefly mentioned in the previous chapter NML is not a technology based on the movement and storage of electrical charges. In NML the binary information is encoded in the direction of the magnetic moment of small magnetic particles and their magnetic coupling.

When one investigates the magnetic structure of a ferromagnetic particle in detail without any external field, it is not homogeneously magnetized, but a finer structure of differently magnetized volumes is revealed. These differently magnetized volumes are called magnetic domains and are usually several tens of nanometers in size. Depending on the material and also the shape of the structure these domains interact differently with each other. When the particles in question are of a size similar to the size of the magnetic domains, they achieve a single domain state. In this single domain state the particle no longer shows a complicated magnetic structure but is only split in north and south pole and can be characterized by a simple magnetic moment. This domain structures stems from the principle of energy

minimization. The stray field emanating from a particle requires energy, thus a multi-domain structure which reduces the external stray field is energetically favorable (see **Figure 2**).

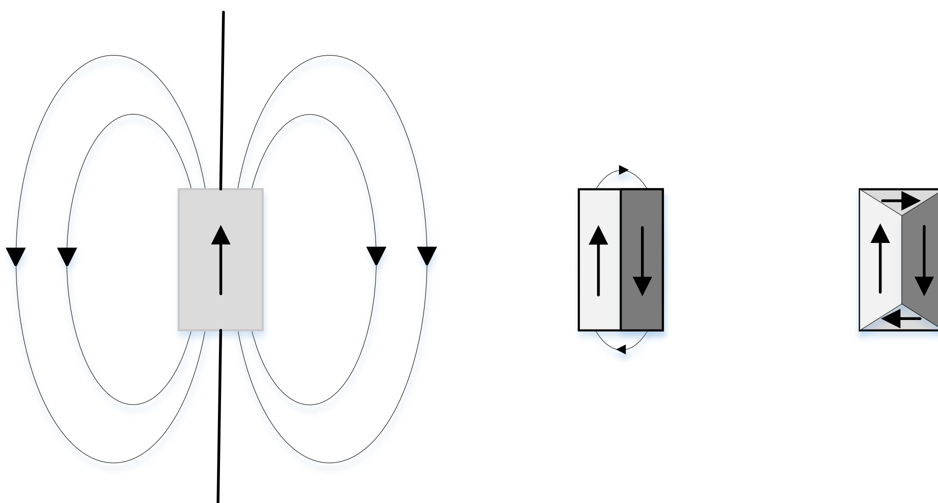

Figure 2 *– Magnetic stray field of different domain structures.The single domain state (left) has requires the most energy for the closure of the magnetic field lines. Increasing the number of domains allows for energetically beneficial internal flux closure but requires energy for the nucleation of domain walls. The actual configuration results from a minimum-sum-balance of these two energies.*

However, between these differently orientated domains a transition zone is established, called a domain wall. This domain wall has a non-zero thickness and inside it the magnetization is steadily rotated to match the bordering domains. This rotation of the magnetization vector however requires energy. Due to this, there is a balance between the single domain state which minimizes domain energy and the multi domain state which minimizes the stray field energy. While the stray field energy is proportional to the volume of the particle (~r^3), the domain wall energy is proportional to its surface area (~r^2). This means that below a certain size limit, typically below 10-50 nm for most ferromagnetic materials, it is energetically favorable for the particle to be homogeneously magnetized. This is called a single domain particle.[15]

The direction of this magnetic moment can be influenced by an external field. After turning off this field the magnetic moment will relax into an energetically favorable direction. Such a direction is called the easy axis of the magnetic particle. It's

opposite; the hard axis is the direction into which the magnetic moment can only be turned by much greater effort. Such different axis can be introduced either by material or crystal structure (crystal anisotropy) or simply by the shape of the particle (shape anisotropy).

Shape anisotropy causes the easy (hard) axis in an elongated particle to fall alongside the longer (shorter) dimension of the particle (see **Figure 3**).

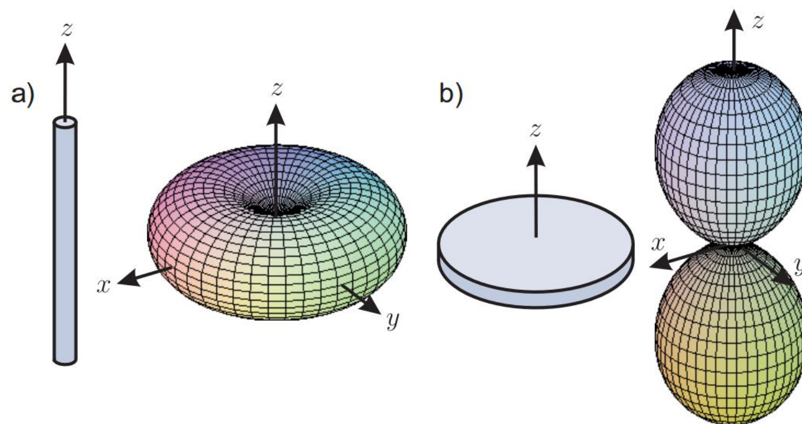

Figure 3 *– Shape anisotropy influence on the magnetostatic energy required for the magnetization of a body. In a) the easy axis of the particle falls along the z axis, while in b) the z axis is the hard axis of the particle. (image taken from [16])*

This creates a bistable state of either parallel or anti-parallel orientation of magnetic moment and easy axis, both energetically favorable and separated by an energy barrier (see **Figure 4**).

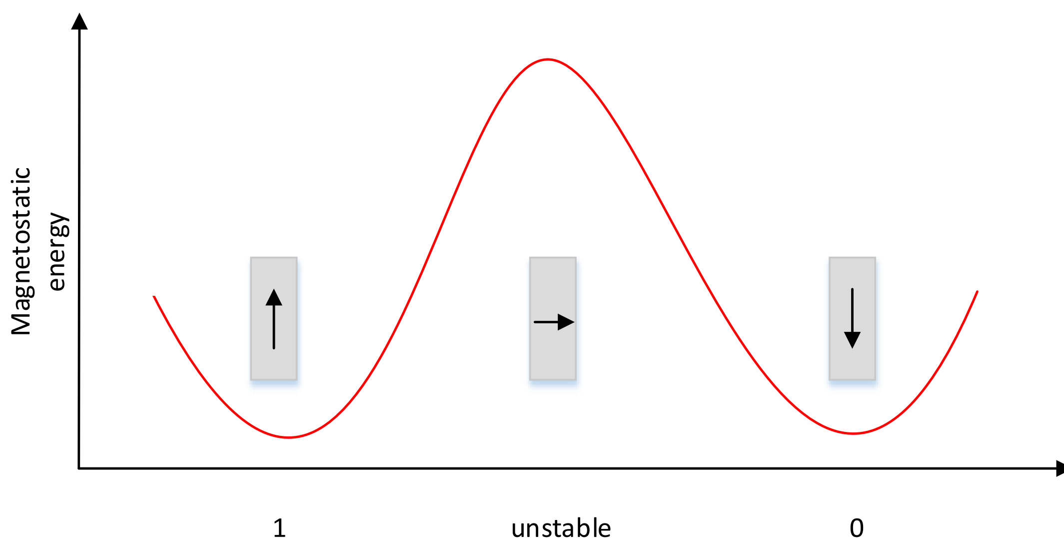

***Figure 4** – Magnetostatic energy in different orientation of the magnetization of a body. Reversing the orientation from parallel to anti-parallel (or vice versa) with regards to the easy axis requires overcoming an energy barrier caused by the shape anisotropy induced requirement for energy to rotate the magnetization vector through the hard axis.*

If this energy barrier is large enough to avoid switching from one state to the other solely due to thermal fluctuation it can be used to encode binary information in a non-volatile way. Via their magnetic stray fields particles in close proximity influence each other and depending on their relative position the coupling between the particles is either ferromagnetic or antiferromagnetic (see **Figure 5**).

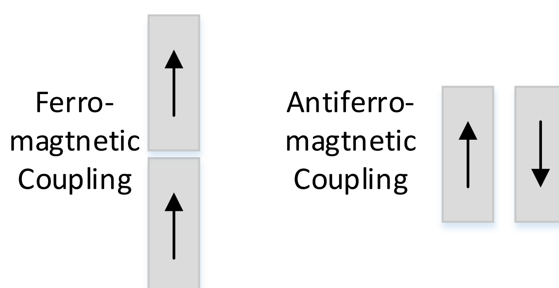

***Figure 5** – Illustration of the nature of ferromagnetic or parallel (left) and anti-ferromagnetic or anti-parallel coupling (right)*

By carefully positioning and shaping of nanomagnetic structures this magnetic coupling can be used to not only store, but also transport and process the binary information. All the magnets except the ones used as input are magnetized along their hard axis by a clocking field. Upon removal of this clocking field the magnetic

orientation of the particles magnetized along their hard axis will relax towards their easy axis. The stray field of the input magnets can influence this process and subsequently lead to parallel or anti-parallel alignment of magnetization and the easy axis. The three main devices in NML are transmission lines ***(i)*** for signal transport, fan-out structures ***(ii)*** for distribution to multiple points and majority gates ***(iii)*** as a basic building block for logic gates. In the following the working principle of these structures is explained using simple two dimensional rectangular nanowire structures.

i. Line

The line structure (see **Figure 6**) is responsible for transporting information between the gates; basically it is the pendant to a wire in electrical systems.

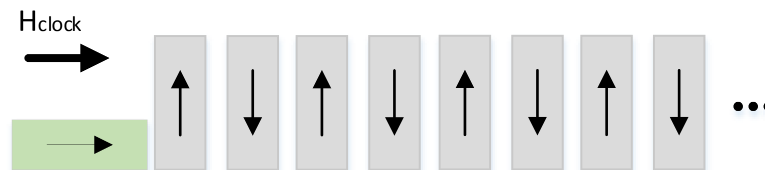

Figure 6 *–Schematic design of a line or wire structure in NML. The horizontal magnet (green) constitutes the input which has its easy axis aligned parallel to the clocking field* H_{clock}*. The vertical magnets (grey) are put in an unstable magnetization state by the clocking field. Upon removal of the clocking field they relax into a state describing binary 0 or 1 as influenced by the ferromagnetic coupling from the input magnet or anti-ferromagnetic coupling from the preceding magnet.*

The input (green) is set in accordance with the clocking field H_{clock} which also magnetizes the perpendicular orientated nanomagnets (grey) along their hard axis. Since this is an unstable state their magnetization would randomly relax into a direction parallel or anti-parallel to the easy axis without influence. Due to the magnetic stray fields of the input structure however, the direction of the relaxation is influenced and the information transported along the 'wire'.

ii. Fanout

The fanout structure (see **Figure 7**) is used to distribute signals from one source to multiple sinks. It basically consists of an input (green) and several helper magnets (light blue) that connect the input to the lines (grey).

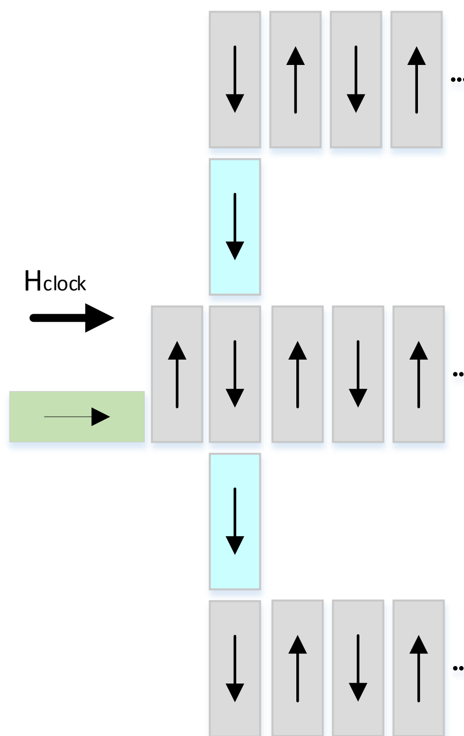

Figure 7 *– Schematic design of a fanout structure used to spread binary signal to multiple sinks.A combination of lines are connected by the ferromagnetic coupling via the vertical helper magnets (light blue).*

iii. Majority Gate

The majority gate (see **Figure 8**) is a three input, one output structure. The output takes the value which is applied to (at least) two of the inputs. The inputs (green) are again set by the clocking field H_{clock} and influence the helper magnets (light blue). The center magnet (yellow) is set according to the majority of the helper magnets and is the only one that is magnetically coupled to the output (red).

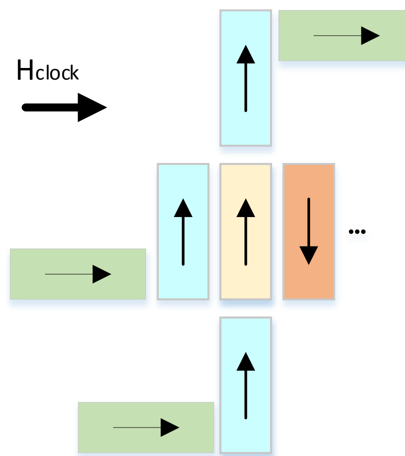

Figure 8 *– Schematic design of a majority gate in NML.The output magnet (red) is only influenced by the anti-ferromagnetic coupling with the center magnet (yellow). This center magnet in turn is influenced by the 3 helper magnets (light blue) in both ferromagnetic and anti-ferromagnetic coupling. It will magnetize according to the majority in magnetization states of the helper and therefore the input magnets (green).*

It can be used as a base gate since it can be used as a NAND or a NOR gate which can be combined to create arbitrary logical functions[2]. By fixing one of the inputs to ‘1’ the gate functions as a two-input NOR gate. On the other hand, by setting one input to a persistent ‘0’, the gate shows NAND functionality.

2.2) Focused Electron Beam Induced Deposition

2.2.1) Motivation

Focused electron beam induced deposition (FEBID) is a maskless, direct-write technology capable of producing two- and three-dimensional structures on the nanometer scale. While it is not (yet[3]) capable of economically viable mass production due to the serial nature of the processes, it is an ideal tool for prototyping

[2] Functional completeness
[3] Several multi-beam systems have been suggested using a multitude of electron beams concurrently, which would allow for swift parallel processing. [42]

and testing of new designs in research and development. This is because structures can be created in a single process step, avoiding complicated and time consuming multi-step lithographic process steps. It is often used to repair photolitographic masks or edit electronic circuits by either etching or depositing material at the desired places.[17] Another use of FEBID is the development, design and prototyping of various nanosystems in sensor technology as well as data storage and processing. [6,18,19]

2.2.2) Basic Principles of FEBID

FEBID uses the electron beam in a scanning electron microscope or a transmission electron microscope for deposition of materials on the nanometer scale. The basic principles of FEBID where observed as early as 1934 by Steward et al. who reported the contamination growth from residual gases (RG) in the SEM chamber [20]. While this was naturally considered a disadvantage that has to be avoided by minimizing the RG in the chamber, purposefully introducing metal-containing gases in the chamber to deposit conductive films was done first in the 1960s by Baker, Christy and Morris [21,22].

The working principle of FEBID can be described as a localized form of chemical vapor deposition (CVD). The precursor gas is introduced into the SEM chamber via a gas injection system. This precursor partly sticks to the surface where it is decomposed by the incident electron beam and its non-volatile parts get deposited on the sample surface (see **Figure 9**).

Aside from the GIS the SEM is also equipped with a beam control to shift the beam in pre-programmed patterns that describe the intended structures. Ideally, after being hit by the beam, the precursor splits into a 'productive' part (*i.e.* the material to be deposited) which binds to the surface and volatile by-products which are pumped away by the vacuum system of the SEM chamber.

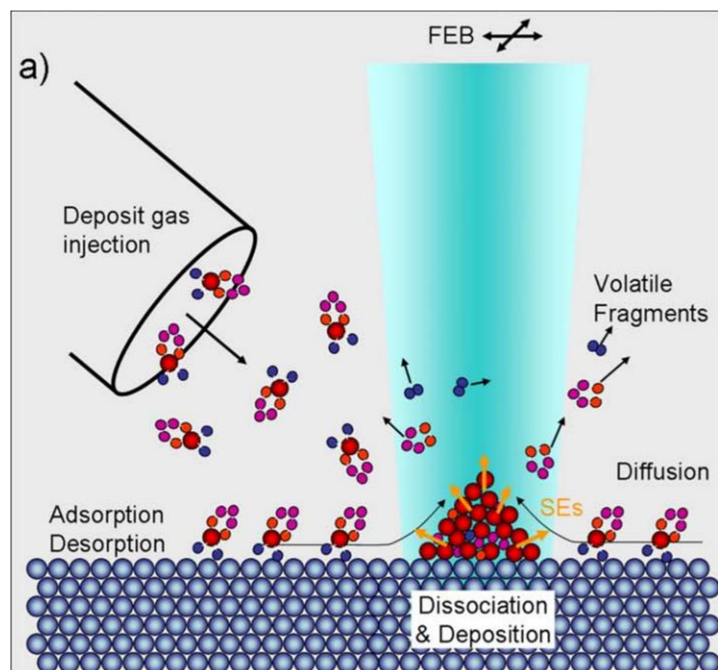

***Figure 9** – Illustration of the FEBID process. The injected precursor gas adsorbs and diffuses on the substrate surface. Parts of this adsorbed precursor desorb again, while the rest gets dissociated into volatile fragments that are pumped away by the vacuum system of the SEM and a 'productive' part that is deposited on the surface. (taken from [10])*

Several kinds of precursors for FEBID exist. For the deposition of metals usually metal-carbonyls ($Me(CO)_x$) or metal-halides (*e.g.* WF6) are used. Because of their relatively simply and clean decomposition the metal-carbonyls are often preferred. Ideally they dissociate into a metal molecule that adheres to the surface and a CO molecule that is pumped away. Unfortunately this is not the always the case and therefore the contamination of the deposited structures by carbon and oxygen is relatively high. While metal-halides usually form much purer deposits they are however much more toxic and corrosive than the carbonyl precursors [10].

There are several important factors concerning the dissociation and deposition of precursor molecules. One of them is the balance between available precursor molecules and available electrons to decompose them at the spot where the focused electron beam impinges on them. If there are more precursor molecules than the electron beam is able to decompose then the deposition occurs in the so called electron (beam) limited regime (ELR). If the opposite is the case, namely when there are more electrons available than precursor molecules to be decomposed at the impingement site one speaks of a mass transport limited or precursor limited regime

(PLR). This balance considerably effects deposition rate as well as the geometry and chemical composition of the deposited materials. The influence of this balance between the regimes on these parameters is discussed in greater details in the results section.

Another factor aside from the actual amount of electrons is their energy. The energy of the electrons can be influenced by adjusting the acceleration voltage of the SEM. This influences not only the beam diameter but also the probability that an electron that hits a precursor molecule leads to a dissociation of said molecule. This is described by the so called electron impact dissociation cross section that can be interpreted as the area that the electron has to hit to achieve decomposition. The maximum of this cross section and thereby the probability to dissociate the precursor molecule is mostly below 100eV. Since this is well below the usual acceleration voltages of several keV it is clear that only a very limited number of primary electrons (PE) from the beam directly decompose the precursor. These PE are scattered elastically on the substrate or the structure itself which results in the so called back scattered electrons (BSE) and forward scattered electrons (FSE) respectively. Inelastic scattering of the PE as well as the BSE result in secondary electrons (called SE1 and SE2, respectively). These secondary electrons are mainly responsible for the dissociation of the precursor, but also negatively influence the achievable resolution due to the fact that they are not limited to the beam diameter but arise in a larger area. **Figure 10** shows simulations by CASINO[4] which demonstrate this fact along with a schematic of the FEBID process.

[4] CASINO v2.48, http://www.gel.usherbrooke.ca/casino/

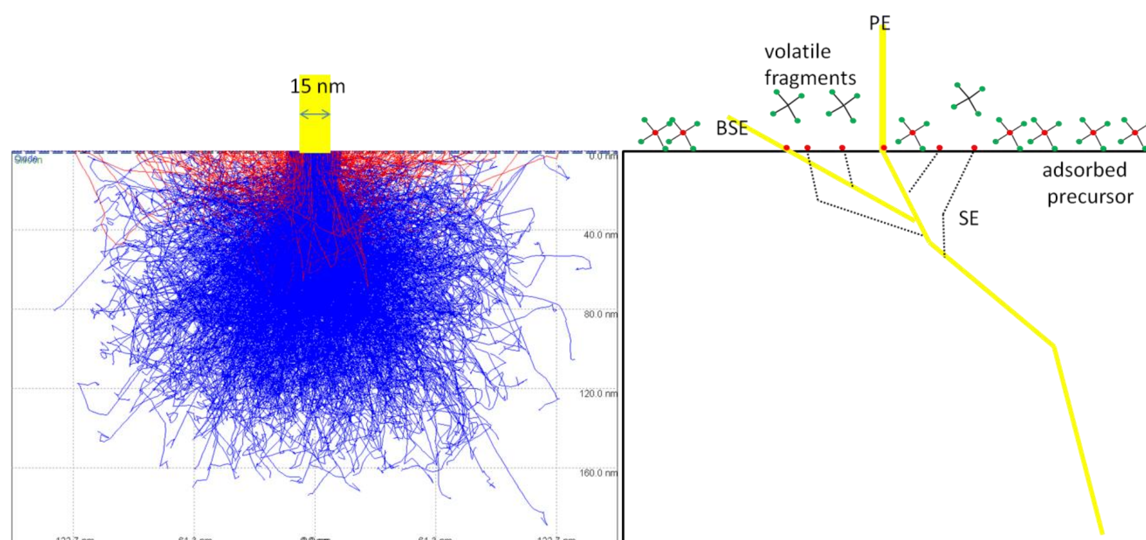

***Figure 10** – CASINO simulation of the electron trajectories inside the substrate using a 3 kV electron beam. This illustrates the emergence of SE and BSE which subsequently dissociate the adsorbed precursor outside the beam diameter, reducing the possibly achievable resolution.*

It is also possible to utilize the same technique to etch away material instead of deposition, called focused electron beam induced etching (FEBIE). The strategy in this case is not to form stable products on the substrate but instead to cause a reaction between the dissociation-products of the precursor and the substrate, e.g. the etching of SiO_2 by using XeF_2. This however is not the focus of this work and should be looked up in other literature [10, 11].

2.3) Characterization Methods

2.3.1) SEM - EDX

Scanning electron microscopy is a technique of microscopy widely used in many fields of science and manufacturing as diverse as nanotechnology and biology as well as the medical sciences. In optical microscopy the maximum achievable resolution is limited by the wavelength of the light used to illuminate the sample. While of course progress has been made by using light of shorter wavelengths, pushing further and further into the UV-band, the use of lenses to manipulate and also the generation of light of such wavelengths becomes increasingly difficult. By using an electron beam instead of light it is possible to avoid the problem of

extreme-UV wavelength light in microscopy. Additionally, the diameter as well as the wavelength of the electron beam used for illumination - two of the main parameters on which the maximum resolution of the system depends - are both much smaller than what is achievable with optical systems, resulting in a resolution of up to 0.5nm. Magnification can be varied over several magnitudes from ~100 to ~1 x 10^{6} .[23]

Instead of optical methods, magnetic and electrostatic lenses are used to focus and move the beam across the surface of the sample, scanning it pixel by pixel until the complete work field is analyzed and a picture is complete.

An SEM mainly consists of a vacuum chamber containing a sample holder and a column containing an electron source and several magnetic lenses for shaping and guiding the electron beam [24] (see **Figure 11**).

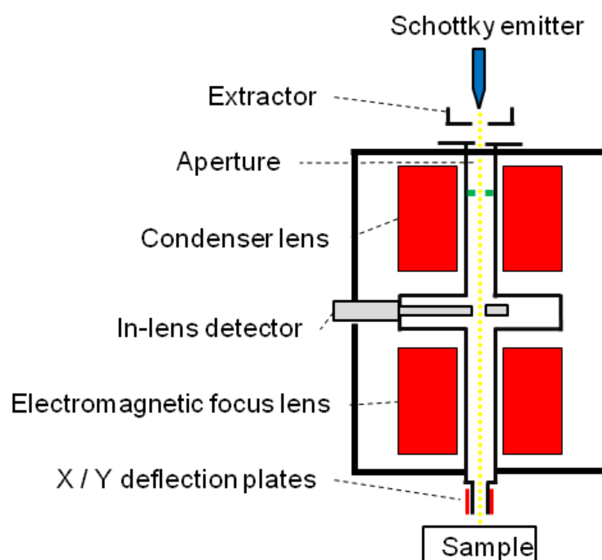

Figure 11 *– Schematic of a SEM column. The electrons are extracted from the Schottky emitter and accelerated by the acceleration voltage. The beam is shaped by the condenser lens and the aperture which functions as a means to control the current. The focus lenses adjust the focal point of the beam to the desired plane on the sample while the electrostatic deflection plates guide the beam in X / Y direction.*

Inserted into either column or chamber are several different detectors specialized to specific particles used to collect information about the sample. The electron beam usually has an energy between 0.5 and 50keV and a current ranging from several pA up to µA. The electrons that form the beam are generated by extracting them from a filament often made from tungsten using thermionic methods, i.e. heat and/or

a strong electric field. These electrons are then accelerated towards the sample by the acceleration voltage forming a beam. This beam is then guided shaped and guided by electromagnetic lenses whose properties can be tuned by changing the current passing through them. As the beam hits the sample it interacts with it in several different ways. The electrons of the beam can be reflected by the sample, forming the so called back scattered electrons (BSE). These BSE as well as the primary electrons (PE) from the beam cause secondary electrons (SE) to be emitted. [25]

Additionally x-rays or auger electrons are emitted caused by the relaxation of molecules that were put in excited states by the electron hitting them. While all of these resulting particles can be used for image creation, often topographical contrast images are formed by detection of SE. The interaction volume of the sample emitting these particles depends on the material as well as the topography of the sample. **Figure 12** shows an example of such an interaction volume. The combination of the extension of the interaction volume and the topography and composition of the sample cause a change in the amount and kind of secondary particles emitted. This is used to create an image of the sample. An illustration of this principle can be seen in **Figure 12**, where the intersection of the interaction volume with an edge causes an increased emission of SE resulting in a high edge contrast in the SE image.

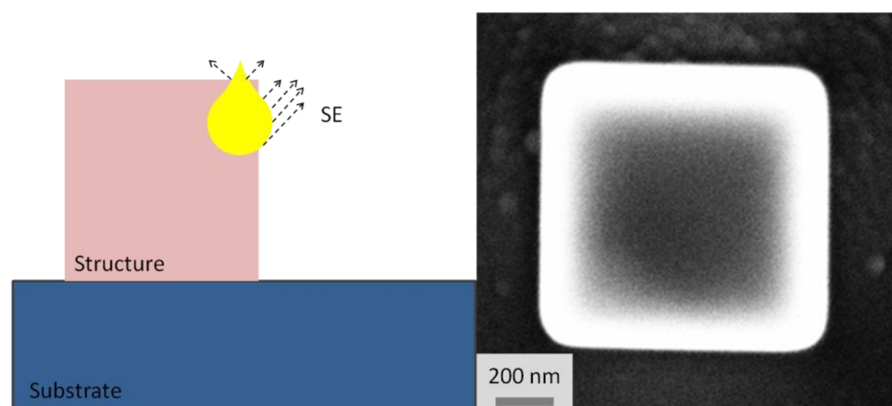

Figure 12 *– Schematic illustration of cause of the edge-effect (left) and an example of it occurring on the edges of a deposited micrometer-sized square pillar (right). On the edge of a structure the interaction volume is no longer contained within the structure itself, leading to an increase emergence of SE and BSE causing an increased signal and therefore an overly bright contrast.*

Since the sample is bombarded by electrons carrying a negative charge, it must be ensures that it is at least somewhat conductive. Otherwise charge will accumulate on certain areas of the sample, leading to distorted images because of coulombic interaction between those charges and the beam. While for metallic samples this is of course not an issue, biological samples are often coated in a thin layer of gold for this reason.

Aside from topographical information chemical composition of a sample can also be determined by a SEM. The technique used for this is called energy dispersive x-ray spectroscopy (EDX). It requires an EDX detector to be installed in the chamber which is an x-ray spectrometer collecting the x-ray photons emitted by the sample and measures their spectral components. Since the wavelength of such an x-ray photon depends on the energy difference of excited and relaxed state of a molecule and therefore on the element-specific structure of the atomic shells, this spectral analysis of the x-rays can yield chemical composition of the analyzed area. This area can be either a spot or as with standard SEM an area comprised of many such spots each forming a pixel yielding an elemental map of the investigated area. [26]

Several important aspects have to be taken into account when performing an EDX analysis. Beam energy must be high enough to actually create excited states, e.g. to detect Fe with its highest spectral peak at ~7keV, more than 7keV in beam energy is required. To perform quantitative analysis a certain number of photons for each wavelength present must be collected to allow for any meaningful accuracy. This of course dictates the time required to analyze a certain part of the sample. This time in combination with the atmospheric conditions in the SEM chamber and the beam current give rise to another problem faced when performing EDX. As mentioned in the previous chapter, the residual gases in the chamber can be decomposed and subsequently deposited on the surface of the sample. Similar to direct damage to the sample structures caused by the beam itself, this parasitical deposition of residual gas increases with the time and the beam current used to analyze an area. The most dramatic effect of such unwanted deposition comes from carbon containing species in the chamber which manifests in an overestimation of the carbon content. It is therefore crucial to perform any EDX measurement in properly cleaned and pumped vacuum chambers.

2.3.2) Atomic Force Microscopy / Magnetic Force Microscopy

AFM is a type of scanning probe microscopy and was developed on the base of scanning tunneling microscopy by Binning et al. in 1986 [27]. It has since become a standard tool in science and has also spawned a huge number of related techniques for application in various fields outside of normal topographical investigation as diverse as e.g. lithography, biology and dopand profile measurement in the semiconductor industry. One of these related methods is MFM.

In AFM, a sharp probe typically made from silicon or silicon-nitride is scanned across the surface of the sample. The forces acting on the probe depend on the distance to the sample. The forces consist of a combination of the relatively long range attractive van der Waals forces, and short range repulsive forces caused by coulomb forces of the overlapping electron orbits of atoms in the tip and in the sample. These forces are usually described using the Lennard-Jones potential (see **Figure 13**).

$$V = \left(\frac{r_m}{r}\right)^{12} - \left(\frac{r_m}{r}\right)^{6}$$

While this is not the most accurate model, it is widely used due to its relative simple computational properties. The negative part of the vertical axis corresponds to an attractive force, while the positive part marks a repulsive regime.[28–30]

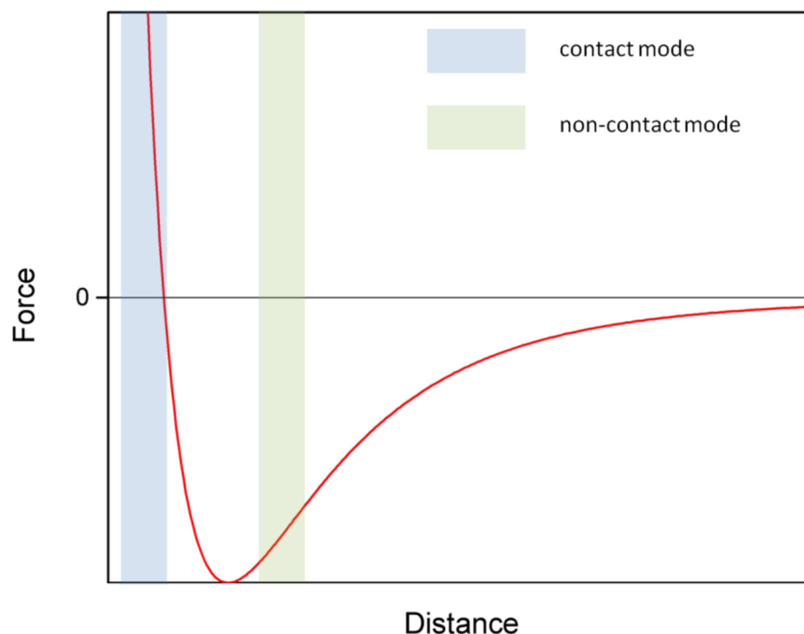

Figure 13 *- Lennard Jones (12,6) potential. This formula is commonly used to describe the interaction between neutral molecules. The positive half-plane indicates a regime of repulsive force caused by coulombic interaction of the molecules while the negative half-plane marks the attractive regime. The contact-mode takes place in the repulsive regime (touching the sample) while the non-contact mode operates farther from the surface in an attractive regime.*

The tip itself is vibrated at its natural frequency. The forces acting on it influence this vibration in frequency, phase and amplitude. The change in frequency can be quantified [31]as

$$\frac{df}{f} = -\frac{1}{2k}\frac{\partial F_z}{\partial z}$$

The mentioned phase is the relative phase-lag between the force-influenced cantilever vibration as measured and the signal driving the vibration at the natural frequency.

This change in vibration is detected and subsequently used to construct a topography image of the sample in combination with the information from stage positioning and the piezo-actuator scanning the tip. This detection is usually done by

focusing a laser on the back of the cantilever (see **Figure 14**) from where it is reflected into a position-sensitive photodetector (optical lever).

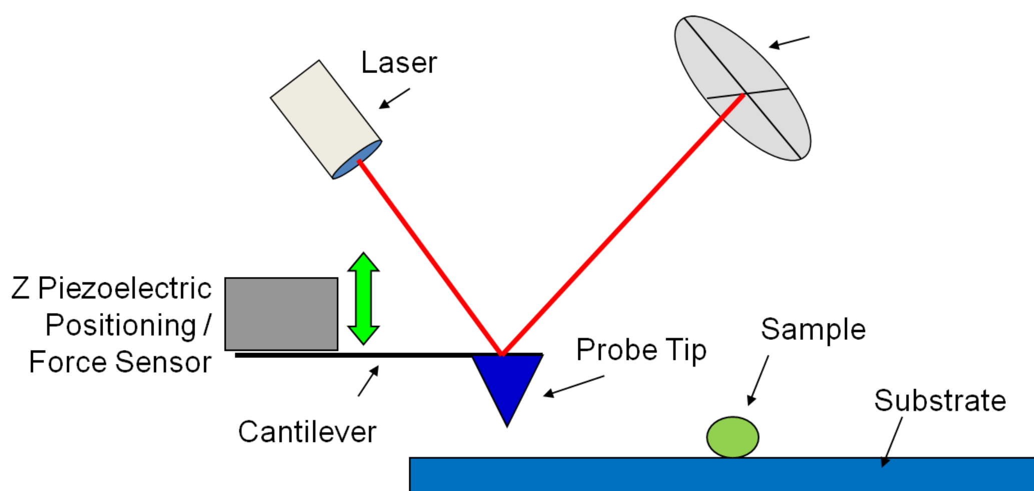

Figure 14 *– Schematic illustration of the optical pickup mechanism (optical lever) used to measure the vibration of the AFM cantilever. A laser is reflected off the back of the cantilever onto a segmented photodiode. This allows for a accurate measurement of the amplitude, frequency and phase of the cantilever-vibration.*

A feedback mechanism keeps the tip at a constant height for force information, or at constant force, which yields the height information. Both eventually can be used to form a topography-image of the surface.

Several different modes of operation are possible (see **Figure 15**) depending in which part of the Lennard-Jones potential the tip is positioned as also indicated in **Figure 13**

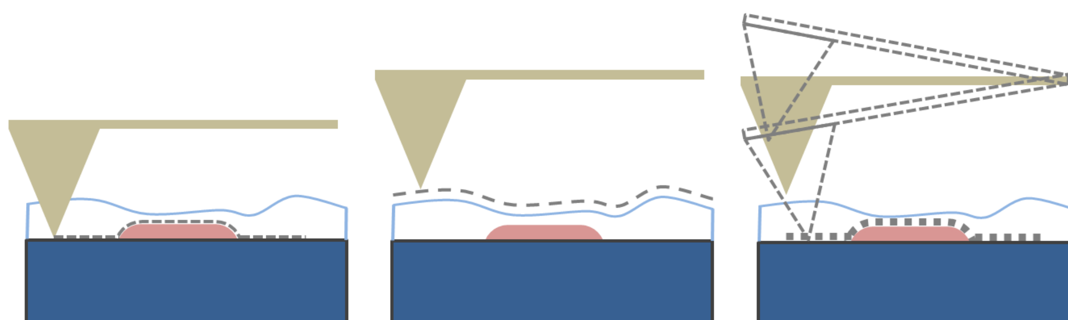

Figure 15 *– Schematic illustration of the different AFM modes. Contact mode (left), the tip is in direct contact with the sample which avoids artifacts from the water layer, but can damage the sample. The non-contact mode (center) does not touch the sample, but the water layer is influencing the image. In the tapping mode (right) the tip is further away from the sample and vibrated at a larger amplitude, only intermittently touching (tapping) the sample. This penetrates the water layer but is not gentle enough to not damage the sample.*

The contact mode, as the name suggests, operates very close (*i.e.* touching) to the sample, in the repulsive force regime. The advantage of this mode is the ability to image a surface with little influence from any adsorbed contamination, which in the form of water is basically constantly present in ambient conditions. Contact mode however, has a significant disadvantage - the direct contact can cause damage of tip and/or sample. Non-contact mode operated further away from the sample surface in the attractive regime. Naturally, in this mode there is less chance of damaging tip and/or sample, but also a greater influence from adsorbed species on the surface. The tapping mode also operates at larger distances but the vibration of the tip has significantly larger amplitude (~100nm) which causes the tip to intermittently touch the surface. This touching however causes far less damage than permanent contact, while being relatively independent from adsorbed species and can even be performed in liquids [29, 30].

The tip itself is usually made from silicon or silicon nitride and aside from a millimeter sized bulk for handling is around 30 µm wide and 100-200 µm long. The standard geometry in AFM tips is a pyramidal shape on the end of this cantilever, whose apex is ideally a single atom. Other shapes like pillars, tilted structures, etc. are also commonly used. Tip geometry is of course crucial, since it massively influences the scan-able features. High aspect ratio structures or pits are often problematic because the tip is unable to completely trace their outline without improper contact due to tip areas other than the apex (see **Figure 16**). This can, just like a damaged tip, lead to artifacts in the image. One is rather 'imaging the tip itself' instead of the structures on the surface. Practically these artifacts are often not easy to discern. They often present in structures resembling tip geometry and can be confirmed to be artifacts by changing scan size since such artifacts do not scale with ‘magnification’.

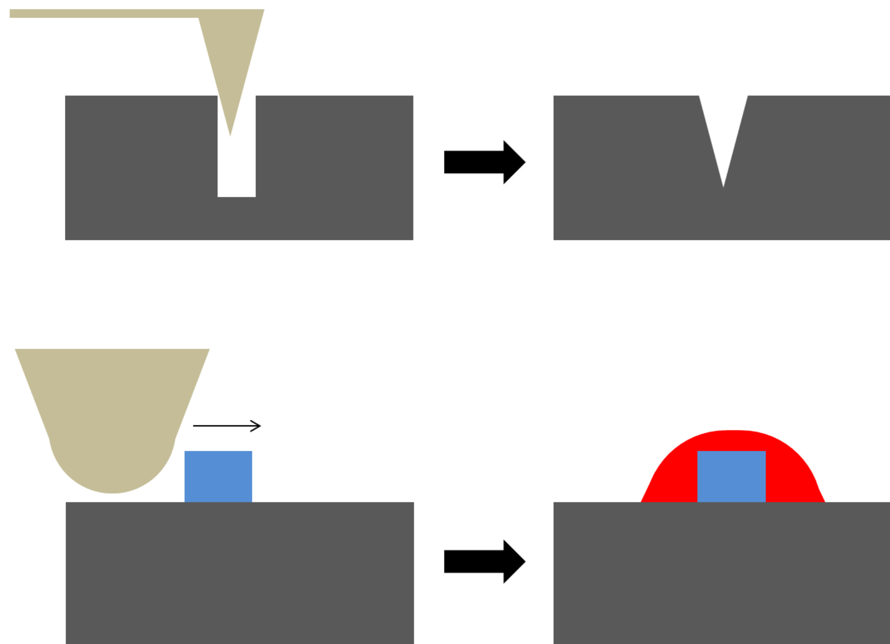

***Figure 16** – Schematic illustration of common AFM artifacts. Narrow trenches where the tip can not reach the bottom are imaged as a negative of the tip shape itself (top). The finite size of the AFM tip does not allow to image smaller particles because the tip is unable to accurately trace their outline. The resulting image is a convolution of tip and structure.*

Magnetic force microscopy (MFM) basically is a magnetic sensor on the nanoscale. It is one of the most successfully used magnetic imaging techniques in nanotechnology. The first MFM was demonstrated shortly after the first AFM in 1987 [28]. It is mostly used for the imaging of the magnetic domain structure of various magnetic materials, such as magnetic recording media (hard disks), thin films, patterned media, etc.

MFM basically uses the force sensing capabilities of an AFM to locally detect the forces acting on a small magnet (the tip) when it is brought in proximity to magnetic structures on the sample. The tip can be described as having a small magnetic momentum $\vec{m}$, which in a magnetic field experiences a resulting force of

$$\vec{F} = (\vec{m} * \vec{\nabla})\,\vec{\mathrm{B}} \qquad \text{or rather} \qquad d\vec{F} = (d\vec{m} * \vec{\nabla})\,\vec{\mathrm{B}}$$

for a small part d$\vec{m}$ of the tip or a zero dimensional point approximation. In this formula lies one of the great challenges of MFM. Since the magnetic forces acting on the tip are long ranged interactions, every part of the tip interacts with the magnetic field and causes a small $d\vec{F}$ influencing the measurement, as opposed to conventional AFM where (except for the case of artifacts) only the apex of the tip is influenced. While the ideal, or simplest, tip is approximated as a zero dimensional point, the actual tip naturally has a certain volume. This volume should be in a single domain state. However, this is often not the case. Domain structure of the tips is often largely unknown and can also be influenced by the sample itself. One usually only knows the global magnetization direction of the tip - along its easy axis and either upwards or downwards with regards to the sample. Since this means that in MFM a volume of largely unknown domain structure is interacting with an unknown magnetic field, MFM is a largely qualitative technique. The main use lies in revealing the direction of stray fields emanating from the sample and from there on the magnetic domains of the structures on it. However, research into making MFM a quantitative measuring tool is ongoing [32–35].

A crucial part of the MFM process is the separation of magnetic forces and molecular forces or topographic influence. In order for this to work, a line of pixels is usually scanned multiple times. During the first scan, a conventional topographic AFM is performed, revealing a profile of the surface. This is done in tapping mode, where the tip intermittently touches the surface and the repulsive force is much larger than any contribution from magnetic fields (see green and yellow path in **Figure 17**).

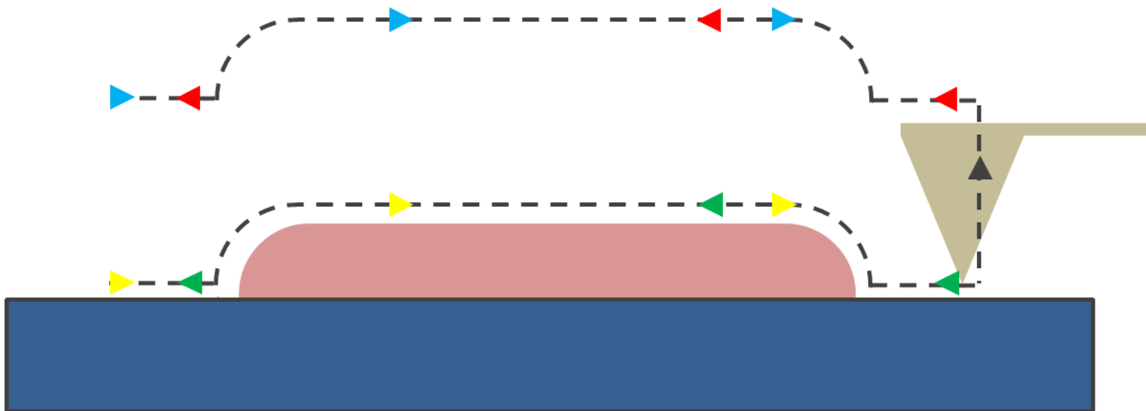

Figure 17 *– Schematic illustration of the MFM process. The tip first takes a topographical image in the tapping mode (trace (green) and retrace (yellow)) and is subsequently lifted to exclude any topographical influence. The tip then is scanned (trace (red) and retrace (blue)) at this height adjusting following the previously acquired topographical profile (constant distance). At this height only long range magnetic forces influence the tip, creating a phase contrast.*

After this first scan, the tip is lifted to a certain height above the sample (~100nm, black arrow) and is then again scanned across the same line while following the profile obtained in the first scan i.e. at a constant distance from the surface (see red and blue path Fig. 6). Since this lift height is rather large, short ranged atomic forces are no longer influencing the tip and the only forces acting on it are caused by the magnetic stray field. The parameter of the lift height is one to carefully optimize, when scanning to high one will only get a very weak signal, while scanning too close causes increased topographic influence (especially when dealing with high aspect ratio structures).

3) Experimental

3.1) Fabrication

3.1.1) LEO 1530VP

The system used for all the depositions was the LEO 1530VP from Carl Zeiss GmbH (see **Figure 18**).

Figure 18 *– Photograph of our SEM system used to perform FEBID. Several GIS can be seen mounted on both right and left side of the chamber.*

The electron beam is created in the column using a Schottky field-emission gun with an extractor voltage of 5.3 kV. The acceleration voltage (V_{acc}) can be adjusted from 1 kV up to 20 kV. The beam current (I_{Beam}) can be adjusted using a multi-hole aperture plate by deflecting the beam to pass through the desired hole, allowing only the desired amount of electron to reach the sample. Using a condenser lens the current can be further increased by narrowing the beam and thereby passing more electrons through the aperture (high current (hc) mode). **Figure 19** shows the

dependency of the electron beam current I_{Beam} on the aperture diameter and acceleration voltage $V_{acc.}$

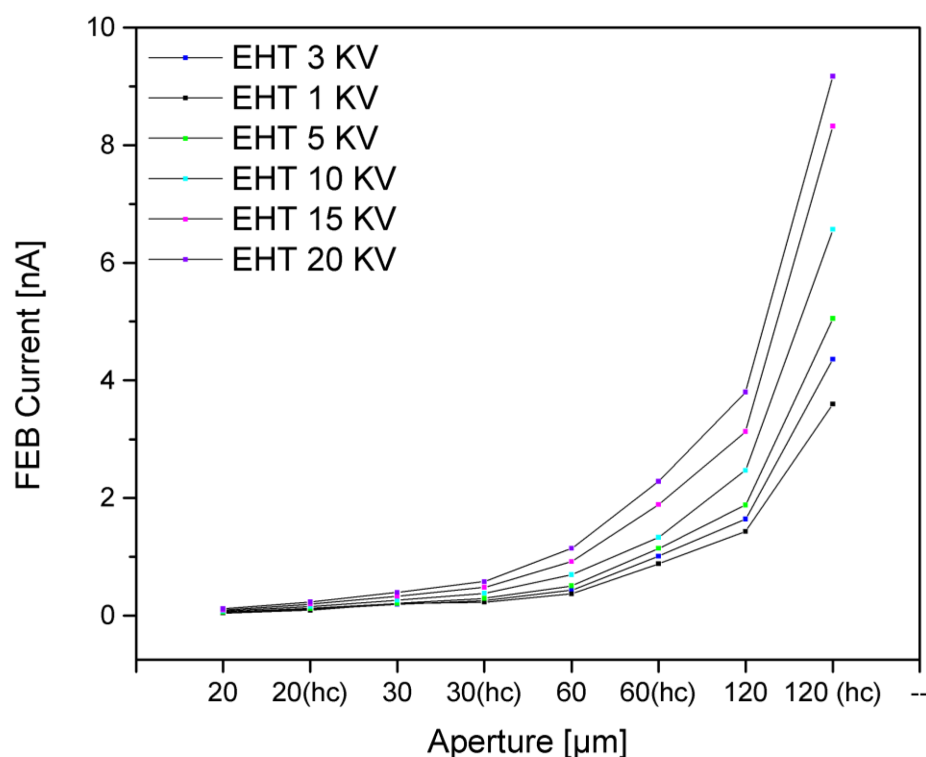

Figure 19 *- Electron beam currents measured at combinations of all SEM apertures and several acceleration voltages.*

Using previously attained results by Dr. Marco Gavagnin, the best parameters for deposition were $V_{acc\,=}$ 3 kV and $I_{Beam\,=}$ 1.0 nA (the standard conditions used unless otherwise stated), which corresponds to using a 60 μm in hc-mode. Beam diameter (FWHM) measured at these values was roughly 14 nm.

3.1.2) The Gas Injection System

The purpose of the gas injection system (GIS) is to supply the precursor to the chamber of the SEM in a stable and controllable way. For the investigation using a

carrier gas a special GIS was custom built in cooperation with Dr. Gavagnin. While there are two commercial GIS capable of carrier gas supported precursor injection, the OmniGIS and its successor the OmniGISII by Oxford Instruments, these systems are significantly more complex to operate and also very much more expensive than our self-built GIS. **Figure 20** shows a schematic of the GIS.

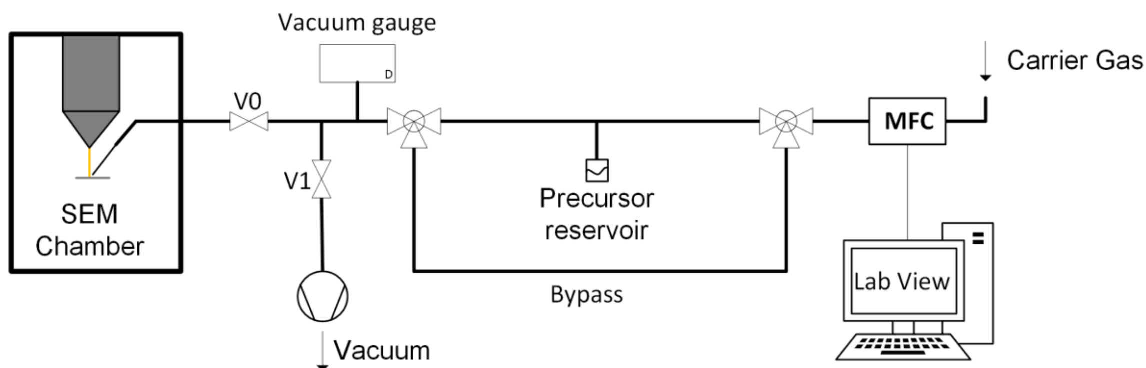

Figure 20 *– Schematic of the carrier gas enhanced GIS used in the experiments with Co_2CO_8. The MFC that is controlled by an external Lab View program injects the desired amount of carrier gas increasing the precursor flux towards the SEM chamber. The bypass line in combination with the auxiliary vacuum pump allows for easy purging and cleaning of the GIS, avoiding multiple purge cycles and compromising the SEM chamber vacuum (V0 closed, V1 open). During deposition procedure itself the bypass line as well as the auxiliary vacuum is not used (V1 closed, V0 open)*

The mass flow controller (MFC) is used to control the flux of the carrier gas entering the GIS line. A thermal based MFC by MKS (MKS-M330) was used that was calibrated for nitrogen gas. While not perfectly accurate due to non-linearities, conversion tables for other gases are available from MKS[5]. For the non-nitrogen carrier gases used, hydrogen and oxygen the deviation in measured flux is expected to be around 1% and has been factored into the values stated in further chapters. Using the three way valves it is possible to guide the carrier gas either towards the precursor reservoir or towards the bypass-line. After these two lines the gas flow can be directed towards the SEM chamber or pumped away by an auxiliary vacuum pump. This, in combination with the bypass line allows easy efficient purging and cleaning of the GIS and precursor reservoir without influencing the atmosphere inside the SEM chamber because it avoids using the SEM's turbomolecular-pump

[5] http://www.mksinst.com/docs/UR/MFCGasCorrection.aspx

(TMP) for pumping away residual gas contaminations inside the GIS. During normal deposition the gas flows from the MFC over the precursor reservoir towards the SEM chamber. The bypass line is closed off as well as the auxiliary vacuum pump (V1 closed, V0 opened).

The GIS consists of 1/4 inch stainless steel tubing and two/three-way ball valves connected by Swagelok stainless steel fittings. The GIS enters the SEM chamber via a flange where it is connected to the nozzle via PTFE tubing. The nozzle itself is made from stainless steel and roughly 30 mm long and has diameter of 0.650 mm. The nozzle is angled 35 degrees relative to the sample plane. Its X position is controlled by a step motor operated by a Lab View program, while Y and Z axis are adjusted manually by positioning screws inside the chamber.

The deposition of iron was performed using a different GIS and an identical nozzle design. The GIS used for iron deposition is comprised of a stainless steel reservoir containing the precursor, a turnstile valve allowing closing of the reservoir and a subsequent needle valve which allows a fine adjustment of the precursor flux reaching the chamber. An auxiliary vacuum pump allows purging of excess precursor and contaminations inside the GIS line without compromising the vacuum of the SEM chamber and the TMP (V0 closed, V1 opened) (see **Figure 21**). Since iron has a far larger vapor pressure (~37 mbar at room temperature), the GIS used for iron deposition does not require heating or carrier gas to increase the precursor flux. Injection of the iron precursor actually requires limiting the flux by using a needle valve. During iron deposition the needle valve was set for a pressure of 2.2 mbar inside the GIS line.

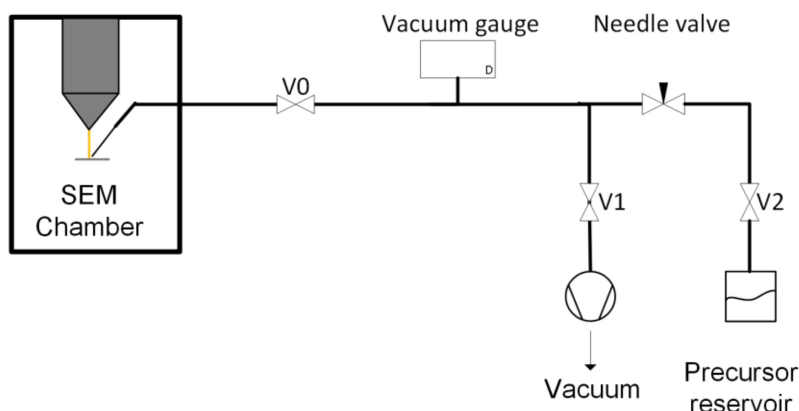

Figure 21 *– Schematic of the second GIS used in the experiments with $FeCO_5$ for the synthesis of NML structures. With this precursor there is no necessity for a carrier gas. The precursor flux is limited by a needle valve. Again, an auxiliary vacuum pump is used for purging of the GIS line.*

3.1.2) Pattern Generator

The task of guiding the beam in the desired patterns was accomplished by using a Raith ELPHY Plus pattern generator. This system communicates with the SEM software and guides the beam in accordance to the pre-drawn patterns (GDS files) that shape the structures. It is usually used for the exposure of photoresist in lithography but also is useful for FEBID applications. While the SEM software offers a macro function to guide the beam in pre-programmed patterns, this system is far more versatile and convenient to use. To achieve a correct deposition of one's structures however, several important parameters must be chosen.

- **Writefield Size**

  This parameter defines the size of the (usually) square working field in which structures can be written. It sets the magnification of the SEM to the value resulting in a full-screen picture of this size.

- **Step Size (Point Pitch, PoP)**

  The step size describes the minimum movement of the electron beam, or the minimum distance between exposed spots. It could also be interpreted as the size of a pixel. The entire writefield is divided into 65536 steps/pixels due to the 16 bit DAC in the beam controller. The minimum step size is therefore limited to

$$minimum\ stepsize\ = \frac{writefield_width}{65536}$$

Usually, the step size is chosen smaller than the beam diameter to achieve a smooth line exposure.

- **Dwell Time (DT)**

  The dwell time defines how long the beam spends on a single spot before moving on to the next spot in the defined structure. This parameter, in combination with the settling time, can be exploited to change the regime of the growth. Depending on the speed of the diffusion of the used precursor, using a long dwell time can possible lead to a depletion of the precursor in the immediate vicinity of the beam. This would result in a deposition in the precursor limited regime. It can be set separately for areas, lines and dots. Due to unknown reasons the software seems to become highly unreliable when choosing values higher than DT_{point} ~8 ms or DT_{line}~0.25 ms.

- **Exposure Loops (Scan Loops, SL)**

  This parameter defines how many times the active layer should be exposed. It can be used to expose designs for a longer time which can be problematic due to charging effects. In our case it was used because the structures required a longer exposure than the pattern generator could reliable provide in a single step.

- **Matrix**

  When trying to minimize beam shift between subsequent exposures (e.g. to minimize drift for the pillars in the NML gates), one should rather use the direct way of actually repeating the exposure by drawing several structures on top of each other during the GDS design instead of the SL parameter. This can be conveniently done using the so called matrix function of the software. However, great care has to be taken to draw the structures in the correct order. One can also set a varying dose factor for each element of the matrix which basically multiplies the DT for this single structure. The reliable maximum that was used for this dosefactor was 7.906.

- **Settling Time**

  The settling time, which can again be separately set for areas and lines or dots defines the time the beam will wait until it writes the next element i.e. the next line or the next area. While being necessary to stabilize the beam, in the case of FEBID it is used to allow the precursor to diffuse to the deposition site.

In the following table the chosen parameters for the depositions are listed in the following table.

	Writefield	**PoP**	**DT (point/line)**	**SL**	**Settling Time**
Squares	15 x 15 μm^2	5 nm	8 / 0.2048 ms	20	10 ms
NML	15 x 15 μm^2	3 nm	8 / 0.2048 ms	30[6]	10 ms

Table 1 *- Pattern generator parameters used for the deposition of the structures*

Furthermore, the software allows for dividing the structure into different layers that can be separately exposed. Using this, deposition parameters and/or the order in which certain parts are deposited can be varied.

3.1.3) Substrate

All structures were deposited on a flat substrate made from Si(100) roughly 15 x 15 mm^2 in size. For the purpose of easy identification, investigation and documentation the substrate was pre-structured using image reversal lithography. After application of AZ5214 photoresist by spincoating and pre-bake (60 s, 100 C), the sample was exposed to UV light (285 nm) to transfer the pattern of the mask into the resist. Following a post-bake at 120 C which causes the sensitivity reversal of the photoresist the sample was flood-exposed to UV light for 13.5 s. Developing of the photoresist took place in tetramethylammonium (TMHA) for 70 s, removing the photoresist in all the areas to be subsequently etched by reactive ion etching

[6] SL = 1 when the matrix function is used to stack the structures

(Plasmalab System 100, Oxford Instruments). After etching for 50s using an SF6 flux of 20 sccm and an Ar flux of 10sccm, 15 V bias, 50 W of RF power at a pressure of 53.3 mbar and a temperature of 35 C the surface structuring was complete.

The structuring consisted of 9 x 12 alphanumerically marked areas, each again subdivided into 50 x 70 µm^2 rectangular areas identified by an alphanumeric coordinate system (see **Figure 22**).

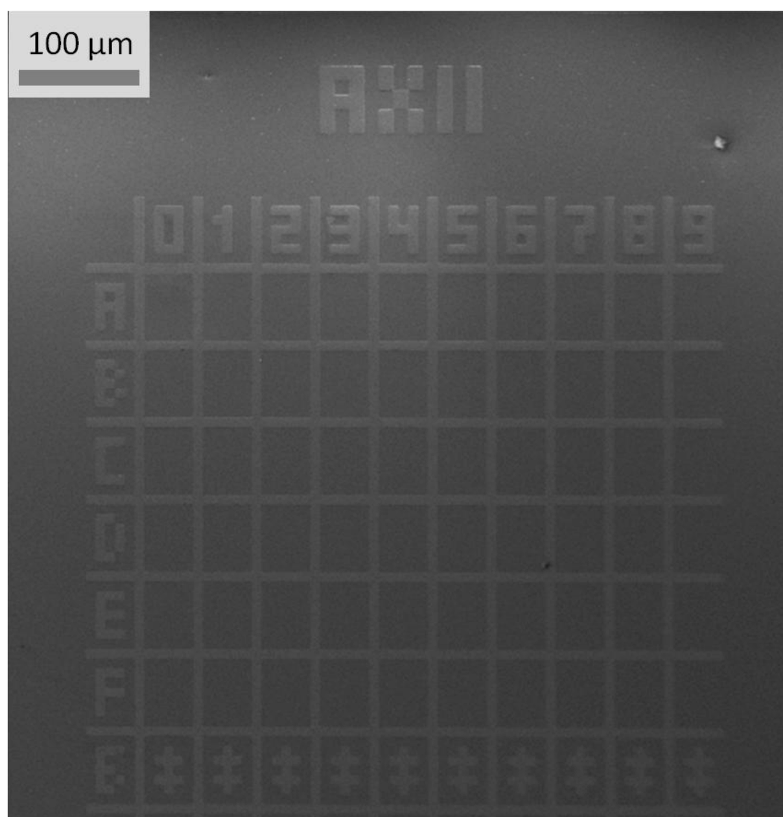

***Figure 22** – SEM micrograph of an overview of the samples alphanumeric pre-structuring by RIE used for locating and documenting the nanostructures in further investigations.*

3.1.4) Design of the structures

3.1.4.1) Carrier Gas Investigation Structures

The structures to be investigated where deposited on the aforementioned 50 x 70 µm^2 areas. To avoid 'cross-deposition' each deposit, although only less than 15 x 15 µm^2 in size, was deposited on a separate area. The structures deposited consisted of a total of four squares, 2 sized 1 x 1 µm and 2 sized 0.5 x 0.5 µm^2 spaced roughly 2 µm apart (see **Figure 23**).

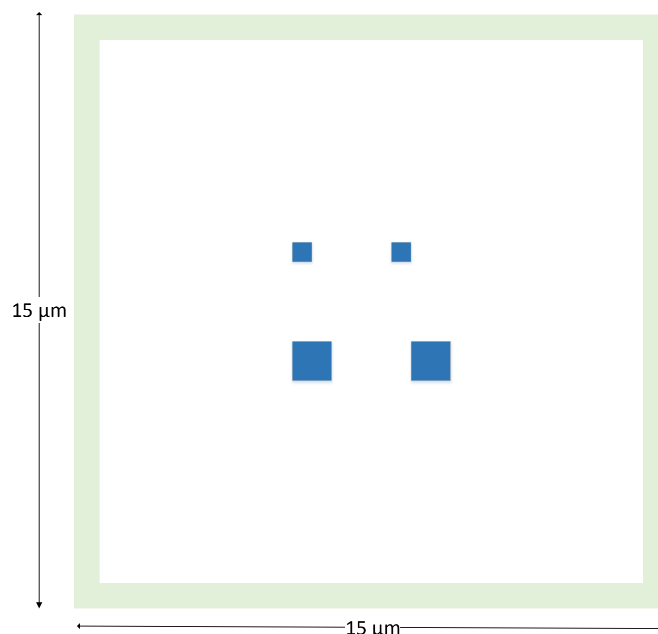

Figure 23 *– Schematic overview of the deposit designs used for the carrier gas investigations. The 15 x 15 µm² is enclosed in a thin frame of deposited cobalt (green) which was found to increase the accuracy of the beam. The structures themselves (blue) are 1 x 1 µm² and 0.5 x 0.5 µm² squares constructed line by line.*

Around the structures, spaced several micrometers away, at the edge of the 15 x 15 µm workfield used for deposition a thin (single pass) rectangular frame was deposited as this was found to increase the accuracy of the beam-guiding. It is presumed this is to the avoidance of charging effects when exposing the central area for extended periods of time.

The squares themselves where actually designed line by line, each consisting of 30 lines to be drawn consecutively on top of each other with a waiting time of 10ms between each line. Thickness of the line, which equals the point-pitch (PoP) or pixel size of the pattern generator was 5nm. Each square deposit consisted of 200 stacks of lines next to each other for the larger and respectively 100 for the smaller squares. This results in the aforementioned area of 1 x 1 µm² for the larger and 0.5 x 0.5 µm² for the smaller squares.

After one complete pass of the 2 times 200 stacks of lines making up both of the 2 larger squares the beam passes over the same area again for another 29 times resulting in a total of 30 scan loops. The complete deposition procedure was then repeated for the smaller squares, resulting in a total deposition time of roughly

12 min for the set of 4 squares. The main deposition parameters are summarized in **Table 2**.

Acceleration voltage	**Beam current**	**Carrier gas flux**	**Base pressure**[7]	**Carrier gas**	**Precursor**
3 kV	1 nA	0 – 0.91 sccm	2.8×10^{-6} mbar	Nitrogen	Co_2CO_8
3 kV	51pA – 4.36nA	0.38 sccm	2.8×10^{-6} mbar	Nitrogen	Co_2CO_8
3 kV	1 nA	0 – 0.46 sccm	3.6×10^{-6} mbar	Hydrogen	Co_2CO_8
3 kV	1 nA	0 – 0.41 sccm	3.7×10^{-6} mbar	Oxygen	Co_2CO_8

***Table 2** – Main SEM and GIS parameters used for the deposition for the carrier gas investigations.*

3.1.4.2) NML structures

The NML structures consist of nanowires and nanopillars arranged to magnetically couple with each other. They were deposited at standard conditions and made from Fe deposited from $FeCO_5$. Iron as a material for the NML structure investigation was chosen because of its straightforward deposition which was well characterized and reliably performed in our lab [3,4] allowing to focus on the structure design instead of deposition optimization. Detailed NML structure design is described in the chapter 5. The deposition parameters used for the deposition of the NML structures are listed in **Table 3**.

[7] Closed chamber valve (V0), i.e. no injection of precursor or carrier gas

Acceleration voltage	**Beam current**	**GIS line pressure**	**Base pressure[8]**	**Carrier gas**	**Precursor**
3 kV	1 nA	2.2 mbar[9]	2.8×10^{-6} mbar	none	$FeCO_5$

Table 3 *– Main SEM and GIS parameters used for the deposition from $FeCO_5$ for the synthesis of NML structures.*

3.1.5 Deposition procedure

After cleaning the sample by ultrasonication for several minutes in acetone and isopropanol followed by a rinsing with distilled water the substrate was mounted on a sample holder and placed in the oven (60 C) to completely dry. After setting the sample holder on the stage of the SEM the system was left to pump for at least 9 hours to ensure a sufficiently low pressure in the chamber. After positioning the stage to roughly 5 mm below the column and setting focus and stigmation the position of the GIS nozzles with respect to the substrate was adjusted. The lateral position of the nozzle was set to 95 µm offset to the right hand side of the center. Vertical distance was set to 100 µm (+-5 µm) by slowly moving the stage upwards in steps of 10 µm while continuously readjusting focus until the nozzle touches the sample followed by a lowering of the stage by 5 µm in order to establish a consistent zero-level. Previous experiments concerning the precursor distribution on the sample plane agree well with the common simulation tool GISSimulator[10] [36] and show the importance of such a careful and consistent nozzle positioning to achieve comparable results.

At this point in the procedure precursor and/or carrier gas pressure was adjusted to the desired levels, as described in section 3.1.2 and left for several minutes to stabilize. Before the first deposition of the series the precursor was opened to the auxiliary vacuum pump at high levels of carrier flux in the case of nitrogen (~1 sccm) or no carrier flux in the case of the other gases to allow purging of accumulated

---

[8] Closed chamber valve (V0), i.e. no injection of precursor or carrier gas
[9] Limited by needle valve
[10] GISSimulator by Utke et al., www.empa.ch/plugin/template/empa/1091

hexane (a stabilizing agent in the precursor) and possible other residual species in the GIS-line for roughly 1 hour. Afterwards focus and stigmation were finely adjusted, which was eased by the edges of the prestructured grid as opposed to clean, smooth substrate. Since the pattern generator resets the beam position to zero beam-shift before it starts deposition, the selection of the deposition site should only be performed using the motorized movement of the stage. After this the system is finally set up and control of the instrument is handed over to the pattern generator which guides the beam, writing the desired pattern layer by layer, taking about 12 minutes for one complete deposition of the carrier gas investigation structures. Following deposition the carrier gas flux was adjusted to the next level and again left to stabilize for ~5 minutes. Repositioning of the stage should again be done only by stage movement instead of beam shifting while keeping the scanning of any previous or future deposition area to an absolute minimum to avoid parasitic deposition. Focus, as well as stigmation should be adjusted after every change in atmospheric conditions inside the chamber, *i.e.* after every carrier gas flux step and also after moving the stage over several micro-areas to ensure a reliable beam profile.

3.2) Characterization

3.2.1) Energy-dispersive X-ray spectroscopy

Chemical characterization of the structures was performed by energy-dispersive X-ray spectroscopy (EDX). After deposition the sample was transferred from the LEO 1530VP used for deposition to a second SEM (Zeiss NEON 40 EsB CrossBeam). This instrument is equipped with a 30 mm^2 X-detector (EDS 7427) by Oxford instruments. Prior to EDX the system was pumped down after sample insertion for at least 10 hours, reaching a base pressure of 1×10^{-6} mbar. Measurements where performed at 5 kV for a duration of 60 s at a distance of 5 mm. Each investigation was performed on one of the larger (1 x 1 μm^2) squares. One of the corresponding smaller squares (0.5 x 0.5 μm^2) was also analyzed as a control value to exclude random fluctuations.

3.2.2) AFM / MFM

Topographical measurements were performed by atomic force microscopy (AFM). The system used was a Veeco/Bruker Dimension 3100 in tapping mode using commercial PPP-NCHR probes by Nanosensors. Each scan analyzed an 8 x 8 μm^2 area, containing all 4 deposited squares. This AFM image was subsequently analyzed by Gwyddion[11]. For the volume estimation a mask was overlaid the square to be analyzed. Great care was taken to keep a consistent mask layout since this is crucial for comparable volume estimation (see **Figure 24**). An error in volume measurement of +-0.02 μm^2 however, is assumed to be present in all measurements.

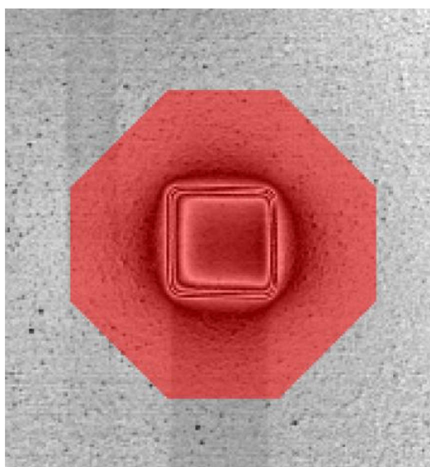

Figure 24 *– AFM micrograph of a square deposited for during the carrier gas investigations overlaid with the mask geometry used for the volume estimation of the deposits. Consistent mask geometry is crucial in order to achieve comparable volume estimations.*

The squares chosen for volume estimation were the ones not used for EDX, since RG in the SEM chamber always leads to a certain amount of carbon deposition, which would have influenced the measured volume. As in the chemical analysis, the volume estimation was performed on a big square as well as a small square for consistency control.

[11] Version 2.28, http://gwyddion.net/

Magnetic investigation of the NML structures was performed by magnetic force microscopy (MFM) using the same instrument. For this, the system was equipped with special, self-made magnetic tips that where magnetized using a permanent magnet with a remanence flux density of B = 12 mT. These tips consist of the same kind of tip as used in the topographical investigation (PPP-NCHR) on which's apex an iron needle was deposited by FEBID. They are ~2 µm long and have a diameter of ~50 nm. Additionally the iron needle is deposited at an angle of 10 (+-2) degrees, which allows to correct the tilt introduced by the cantilever holding system, keeping the tip perpendicular to the sample. **Figure 25** shows an SEM micrograph of such a tip. Details about these tips are awaiting publication by Gavagnin et al.

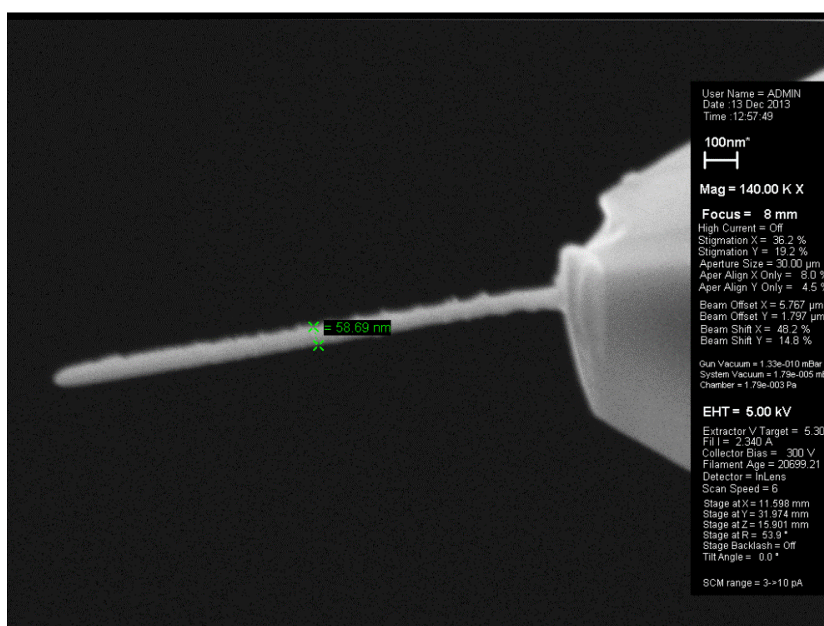

Figure 25 *–SEM micrograph of the FEBID tip used in the MFM investigations. A needle made from iron is deposited on the apex of a (damaged) AFM tip. The needle is roughly 2 µm long and has a diameter of approximately 50 nm.*

Figure 26 shows an example of a topographic AFM scan (a) of an array of orthogonally deposited nanowires, the corresponding MFM (b) and a schematic representation of the magnetic stray-field in (c). These nanowires are approximately 30 nm high and 500 x 100 nm long/wide and were deposited as a sample to measure the coercivity of the FEBID MFM tips. The dark and bright contrast in (b) marks an area of attractive, respectively repulsive force acting on the tip by the

magnetic stray field of the structures. The external magnetization of this sample was done in X-direction at 1.8 kOe. Therefore the horizontal magnet is magnetized along its easy axis and the vertical magnet is magnetized along its hard axis by the external field. Since this is an energetically unfavorable state it will randomly relax into a magnetization direction either along its easy axis. Since the horizontal magnet is already in the stable state it will influence the vertical magnets magnetization by anti-ferromagnetic coupling. In this way the magnetization of the vertical magnet depends on the magnetization of the horizontal one, which is the basic principle of NML.

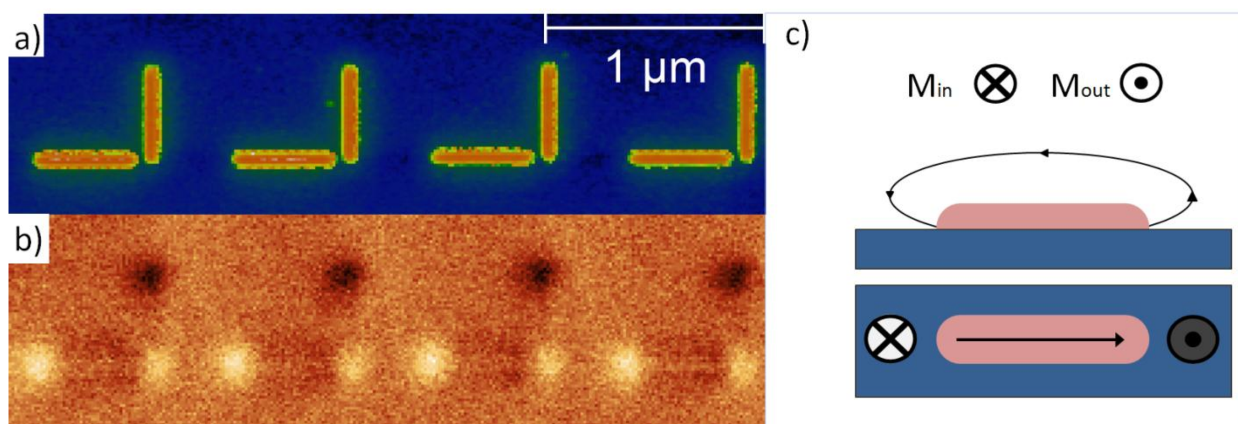

***Figure 26** – AFM (a) and corresponding MFM (b) investigation of a series of perpendicular iron nanowires. (c) shows a schematic of a nanowire and its magnetic configuration. The dark (bright) contrast in (b) represents field lines entering (emerging from) the sample.*

4) Carrier Gas Enhanced FEBID

4.1) Motivation and Overview

In FEBID the commonly used precursors are solid or liquid at room temperature [10,11]. To facilitate injection into the SEM chamber however, the precursor must be in a gaseous state. Many precursors, such as the widely used iron precursor iron-pentacarbonyl ($FeCO_5$) show a sufficiently high vapor pressure to achieve a high enough gas flux by pressure differential between GIS and SEM chamber alone [10,11]. In this case, controlling the flux of precursor is rather simple – an adjustable valve limiting the flux is enough. Some other precursors such as the commonly used WF_6 for tungsten deposition or the precursor used in this work for cobalt deposition, Co_2CO_8, have a considerably lower vapor pressure. Due to this, the evaporation of precursor inside the reservoir is too slow to facilitate sufficient flux into the chamber for controlled deposition [5,12,37–39]. While a precisely controlled precursor flux is very important for deposition, it is absolutely crucial when co-deposition of more than one precursor at the same time is done, where the balance of the two (or more) precursors present at the target is a deciding factor for the characteristics of the deposits.

While the concept of enhancing and controlling the flux of a material by using a carrier gas is a commonly used method in CVD many other areas, in FEBID so far this technique has not been used. Instead, the main strategy used presently is to increase the evaporation by heating the precursor. This however brings several disadvantages, such as the necessity to accurately control temperature along the entire GIS, Nozzle and Sample setup to avoid re-condensation and/or unwanted deposition caused by temperature gradients. The carrier gas strategy avoids any possible temperature gradients since there are no heated elements and everything is done at room temperature. Using the custom built GIS it is possible to stream carrier gas over the precursor inside the reservoir and to the chamber. On the atomic scale, this means that carrier gas molecules are transferring their kinetic energy to gaseous precursor molecules inside the reservoir, giving them directionality towards the chamber. This avoids the saturation of the reservoir with gaseous precursor by keeping the partial pressure of the Co_2CO_8 inside the

reservoir below the vapor pressure, which results in an increased evaporation of precursor at room temperature. The first carrier gas chosen for this experiment was nitrogen. This was done because of the relatively inert properties of nitrogen, which was expected to avoid any direct chemical reactions between the carrier gas and the gaseous precursor, only resulting in increased precursor flux. In order to create cleaner structures other, more reactive carrier gases were also used. The reducing and oxidizing gases hydrogen and oxygen where used in subsequent experiments. Since aside from residual gases in the chamber the source of the contamination of the structures is undecomposed precursor the reactive carrier gases were expected to oxidize/reduce these precursor fragments leaving them to be pumped away by the systems TMP instead of being incorporated into the structures.

4.2) Methods and Experimental Details

Using the carrier gas enhanced GIS a systematic parameter study regarding the carrier gas and its flux was performed. Other parameters were kept constant, if not otherwise mentioned. The carrier gas flux was limited in order to keep the pressure in the SEM chamber below a safe value of 1×10^{-4} mbar. Each deposition was performed at first without carrier gas, *i.e.* 0 sccm of carrier flux. Using the MFC controlled by the Lab View software carrier gas flux was subsequently increased in steps of 0.05 sccm for the following depositions until deposition at the maximum allowed flux has been performed.

Since introducing relatively high fluxes of gas into the chamber of an SEM without destabilizing its atmosphere the first experiment for every series performed was a simple injection of carrier-gas without any electron beam and a closed column-chamber valve to avoid compromising the column vacuum in case of an unstable chamber pressure inside the chamber. Carrier gas was introduced into the chamber along with precursor. After increasing the carrier flux by one step of 0.05 sccm the flux was kept constant for a few minutes in order to allow the pressure to stabilize. This was done for every kind of carrier gas investigated. The results of this investigation are presented in the chapters corresponding to the investigated carrier gas.

4.3) Results and Discussion

4.3.1) Nitrogen as a Carrier Gas[12]

Since Nitrogen is regularly used to vent and flush the chamber it was chosen as a carrier for this first experiment. Keeping the limit of 1×10^{-4} mbar, the highest precursor flux was 0.91 sccm of nitrogen carrier gas corresponding to a chamber pressure of 1.066×10^{-4} mbar. The results of this experiment are shown in **Figure 27**.

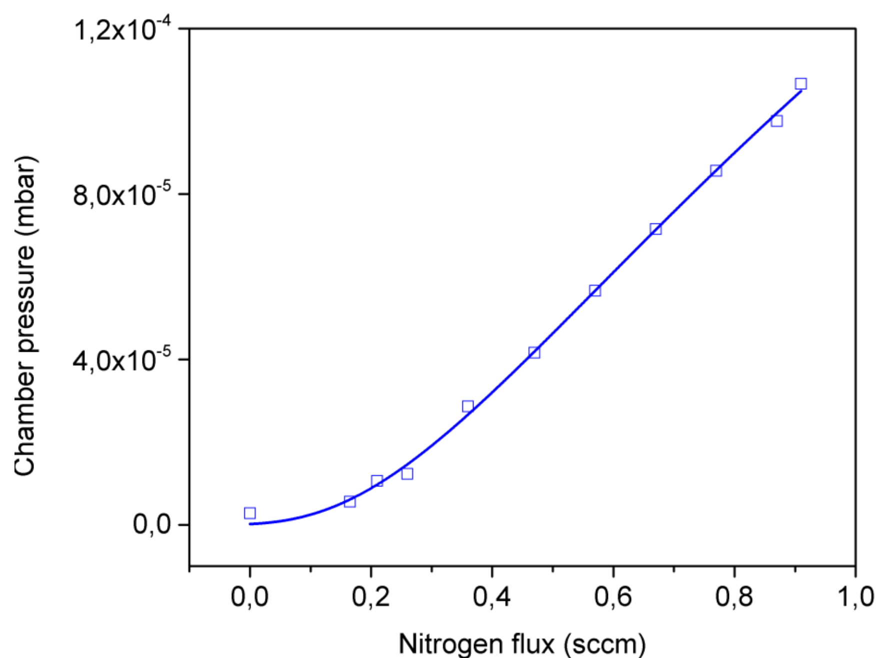

Figure 27 *– Influence of the flux of nitrogen carrier gas on the pressure in the SEM chamber shows good correlation and confirms the possibility of injection of high nitrogen fluxes into the chamber. The base pressure inside the chamber prior to injection (leftmost point) was* $P_{chamber} = 3.4 \times 10^{-6}$ *mbar*[13]

These results demonstrate excellent correlation between the carrier gas flux and the chamber pressure showing the general possibility of injecting large fluxes of nitrogen carrier gas into the SEM chamber without compromising its vacuum or the precursor inside the reservoir. Increased and controllable chamber pressure, however, does

[12] The results regarding nitrogen as a carrier gas for FEBID have been published in [37]
[13] This figure has also been published in [37]

not necessarily imply increased and controlled precursor flux to the sample. To demonstrate this, actual depositions have to be performed.

4.3.1a) Deposition Rate

Deposition was performed over the full range of available nitrogen fluxes (0 - 0.91 sccm) at the mentioned standard conditions (I_{Beam} = 1 nA, U_{acc} = 3 kV). Influence of the carrier gas on the deposition was clearly demonstrated and consistent through several deposition series.

AFM profile measurements of the deposited structures where performed. The results of those are shown in **Figure 28** along with an SEM micrograph and an AFM 3D view of the squares. Deposition is clearly influenced by the flux of the nitrogen carrier gas. The deposits show a nearly 100% increase in height while remaining accurate geometry. The structures also display the 'halo' that is typically formed around FEBID structures by the plume of secondary electrons emanating from the sample surface [40]. The arrow in **Figure 28** c) indicates the position and direction of the nozzle relative to the structures. In d) a close-up of the (ideally) vertical walls of the deposits is shown. On the side of the structure which is facing the nozzle the edges of the walls show a slight round-off which is increasing with higher fluxes. This round off can be explained by shadowing effects, of the precursor flux by the structures as reported by Utke et al. [36] for higher precursor fluxes.

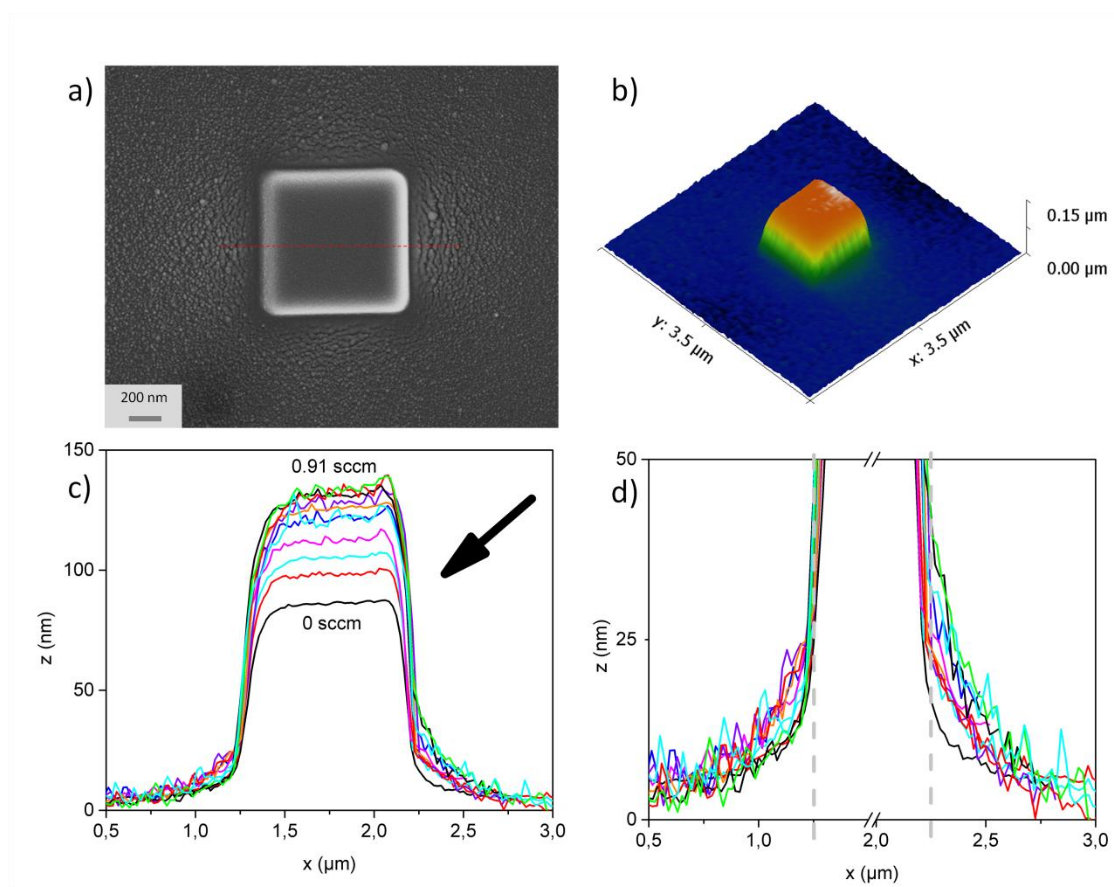

***Figure 28** – Geometrical investigations of the square structures. (a) and (b) show an SEM micrograph of a square and the corresponding 3D view captured by AFM. (c) shows the height profile of a cross-section along the red dashed line in (a) of the deposits synthesized at different fluxes. The arrow in (c) marks the orientation of the GIS nozzle relative to the sample. (d) shows a close-up of the (ideally) vertical walls of the deposits. Shadowing effects on the side of the deposit facing the GIS nozzle are increased at higher fluxes.* [14]

Figure 29 shows the deposited volume of the structures with varying carrier gas flux. Since the deposition rate for the structures remains constant this accurately represents the achieved deposition rate. The deposition rate increases roughly linearly until it saturates at a certain flux level which indicates that the precursor flux is indeed increased by the carrier gas. The saturation at roughly 0.38 sccm of carrier flux indicates a transition from the precursor- or mass transport-limited regime (PLR), where the lack of available precursor is limiting the growth rate to the electron limited regime (ELR) where there is an abundance of precursor and the amount of

[14] This figure has also been published in [37]

electrons is too low to completely decompose it. This confirms the hypothesis that using nitrogen as a carrier gas actually increases precursor flux towards the sample. The composition of the structures corroborates the assumed regime transition. The amount of carbon impurities in the structures are mainly caused by carbonaceous species in the residual gas in the chamber and therefore remain largely constant. The declining cobalt content of the structures as well as the increase in oxygen impurities in the structures indicate the incorporation of undecomposed precursor inside the structures – a characteristic property of the electron limited regime [11,12,41].

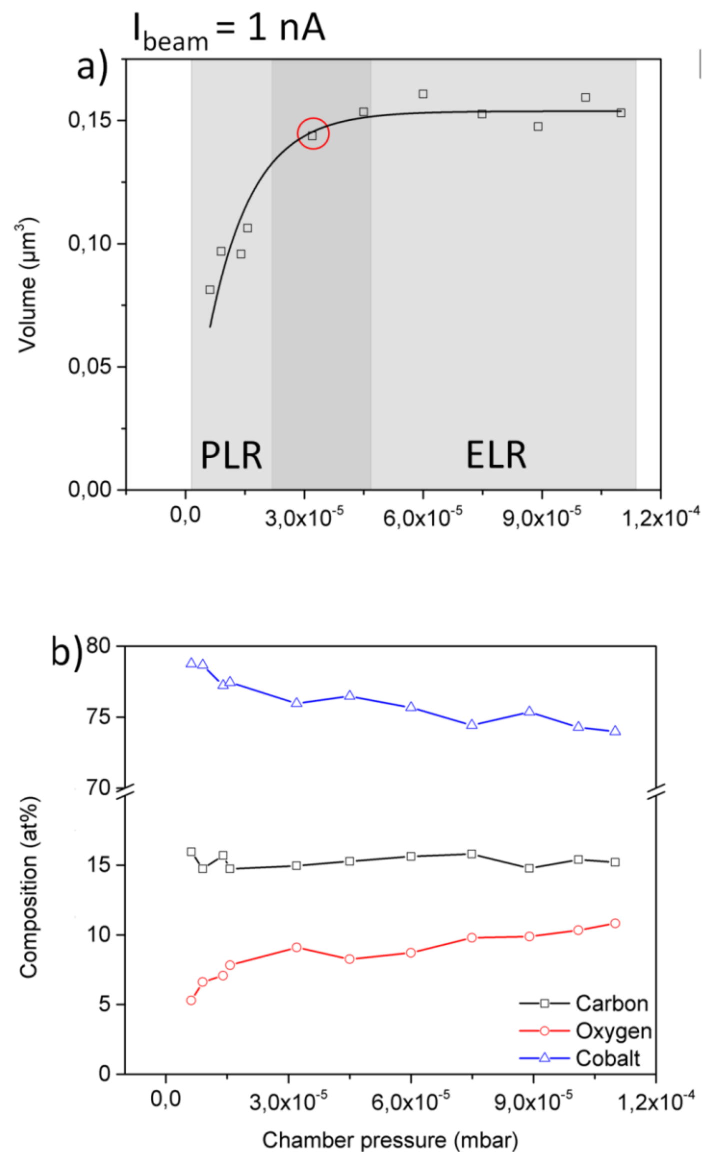

Figure 29 *– Deposited volume (a) and chemical composition trends (b) of the structures deposited at different fluxes of nitrogen. All depositions were performed at I_{beam} = 1 nA. Higher and lower fluxes clearly establish an ELR or a PLR respectively. The transition zone between those two regimes is relatively wide and indicated by the darker grey area in (a). Due to this further experiments varying the electron beam current were performed at the suspected transition point of 0.38 sccm (red circle in (a)).* [15]

This regime change occurred rather gradually and cannot accurately be pinpointed to a certain flux. The transition point must be somewhere between 0.27 sccm and 0.43 sccm, indicated by the darker grey area **Figure 29** (a). To accurately define this

[15] This figure has also been published in [37]

transition a separate experiment was performed at the suspected transition value of the nitrogen carrier gas flux, 0.38 sccm. The carrier gas flux was kept constant at this level and the electron dose was varied by changing the aperture and thereby the electron beam current. This is expected to again show an increase in the growth rate saturating at higher values of I_{Beam} when the deposition transitions from the ELR at low I_{Beam} to the PLR at high I_{Beam}. The 'point of intersection' of this two experiments is marked in **Figure 29** (a) and **Figure 30** (a) by a red circle. The experiments show consistent results and as shown in **Figure 29** (a), growth rate indeed saturates at higher currents, confirming the suspected regime change. It can be seen that the intersection point (0.38 sccm @ 1 nA) now is clearly situated in the PLR. This means that at 0.38 sccm of nitrogen carrier gas flux 1 nA of beam current is more than sufficient to decompose the entire precursor available at the beam impingement spot. Since the transition is now a lot sharper (darker grey area in **Figure 30** (a)) in this experiment, one can deduce that the regime transition point must be at higher carrier flux values, namely between 0.40 sccm and 0.45 sccm. Effects of electron beam induced heating are assumed to be negligible. While these effects certainly have the potential to influence the deposition, any beam heating induced effects reported in literature were when depositing high aspect ratio needle like structures. Since the herein used structures are of planar nature and therefore offer a far greater path for heat conductance allowing them to remain at room temperature [5].

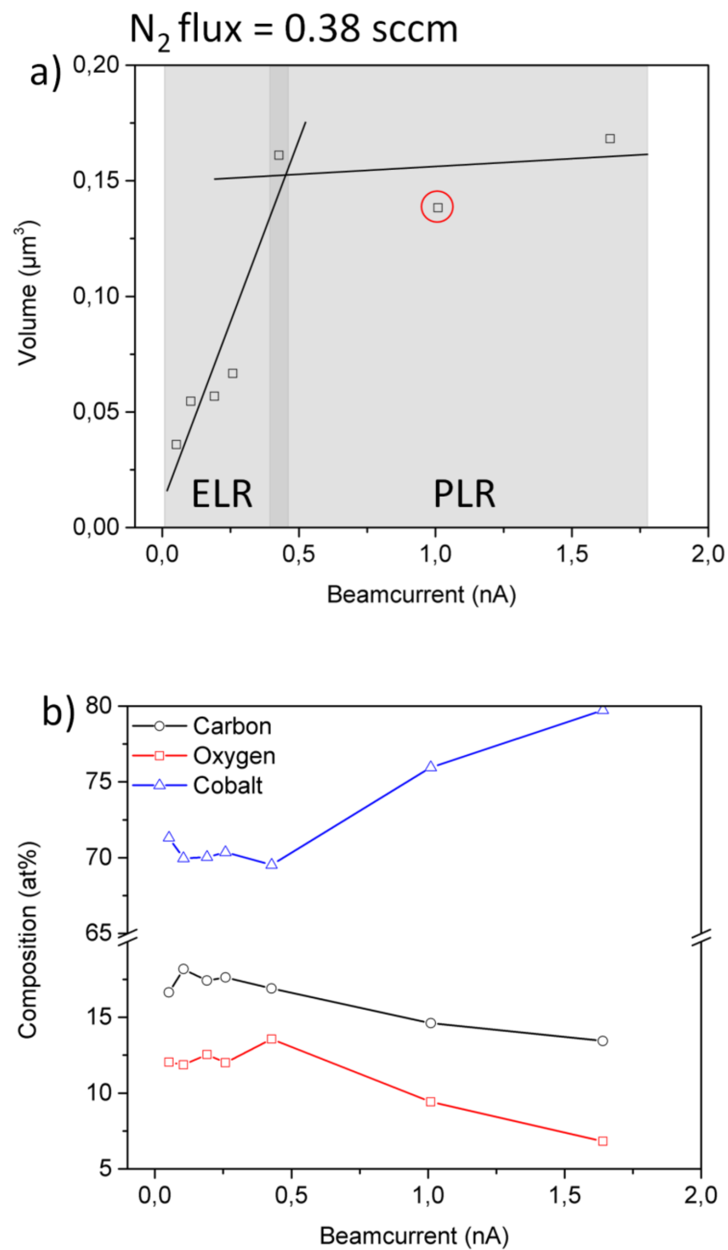

Figure 30 *– Deposited volume (a) and corresponding chemical composition trend (b) of the structures deposited at different beam currents. The point of intersection with the previous flux variation experiment is marked by the red circle in (a). This experiment allowed to more accurately define the transition point from ELR to PLR. It is obvious that the marked point (0.38 sccm) lies in the PLR.*[16]

[16] This figure has also been published in [37]

While nitrogen in principle displays rather inert properties, it is not completely clear whether or not the nitrogen has any chemical effects on the precursor gas. While not expected in this case, it is not known if the nitrogen does not form any chemical compounds with the precursor gas under the influence of the electron beam. To exclude this, the EDX scans were investigated for traces of nitrogen inside the structures. As clearly indicated by the dashed line in **Figure 31** the structure do in fact not contain any nitrogen.

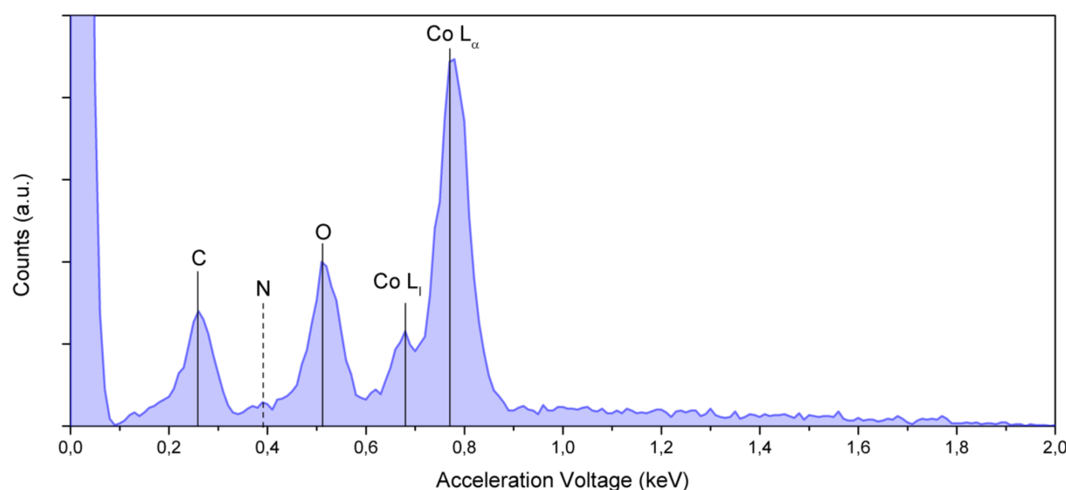

Figure 31 *– Full EDX spectrum of a structure deposited at 0.87 sccm. The absence of nitrogen in the structures confirms the expectation that the nitrogen acts as an inert carrier gas since there are no nitrogen compounds formed even under the influence of the electron beam.*[17]

These findings are one of the main results of this work. The accurate definition and control of the transition from PLR to ELR or inside the regimes provides a key advantage. Usually the PLR enables high purity and well controlled deposition at a certain value of I_{Beam} due to the complete decomposition of the precursor but it is rather slow due to the lack of available precursor. The ELR on the other hand allows the maximum rate of deposition but suffers from a loss in purity due to the inability of the electron beam to completely decompose the precursor whose fragments are incorporated in the structures. Naturally, both properties – quick and pure deposition of material – are desirable. The transition point between those two regimes, which

[17] This figure has also been published in [37]

has been pinpointed in this work, marks what can be considered a ‘sweet spot’ of deposition where there is just enough precursor available to be decomposed by the electron beam. At this point the deposition rate is maximized and any further increase in precursor supply will only create more impurities. The ability to control the deposition regime enables an optimized deposition procedure that allows pushing the deposition towards the maximum deposition without any unnecessary sacrifice in purity.

4.3.2) Hydrogen as a Carrier Gas

As with nitrogen, again an experiment to confirm the possibility of introducing hydrogen carrier gas into the chamber was performed. Again, observing the limit in chamber pressure, the maximum flux of hydrogen carrier gas was 0.463 sccm which resulted in a chamber pressure of 9.01×10^{-5} mbar. Results of this experiment are shown in **Figure 32**.

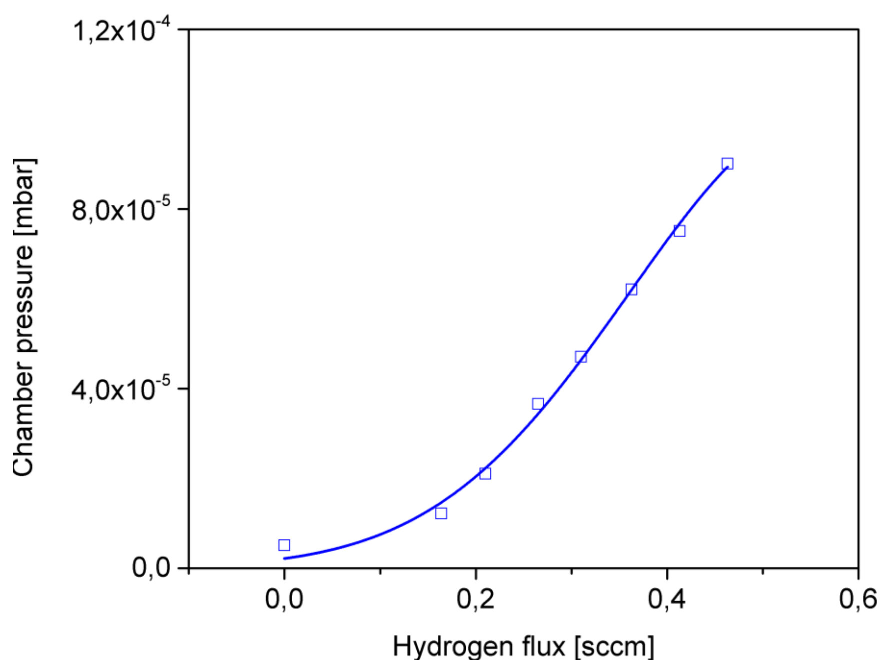

Figure 32 *– Influence of the flux of hydrogen carrier gas on the pressure in the SEM chamber. Changing the carrier flux resulted in a stable chamber pressure after a few minutes. The noticeably lower flux at which the maximum allow chamber pressure is achieved is caused by the much smaller and lighter hydrogen atoms which are far more inefficiently pumped away.*

It is obvious that the flux of hydrogen for the maximum allowed chamber pressure is significantly lower than the flux of nitrogen carrier gas. This is because the pumping of the nitrogen atoms by the turbomolecularpump of the SEM is much more efficient than the pumping of the comparatively very small hydrogen atoms. This results in a lower out-flux of from the chamber, thereby creating a higher pressure than nitrogen carrier gas at the corresponding flux levels. Stabilization of the chamber pressure however, was possible without problems or visible negative effects on the precursor in the reservoir. Therefore experiments with hydrogen were performed as planned.

4.3.2a) Deposition Rate

As described previously, hydrogen as a carrier gas was hoped to have reducing effects on the residual gases and precursor fragments making them more volatile and easier to pump out of the chamber before being incorporated into the structures, possibly leading to cleaner deposits. An experiment was performed in the same fashion as with nitrogen was performed. Depositions were performed with increasing hydrogen carrier gas flux until the maximum allowed pressure was reached. The highest used hydrogen carrier flux was 0.463 sccm.

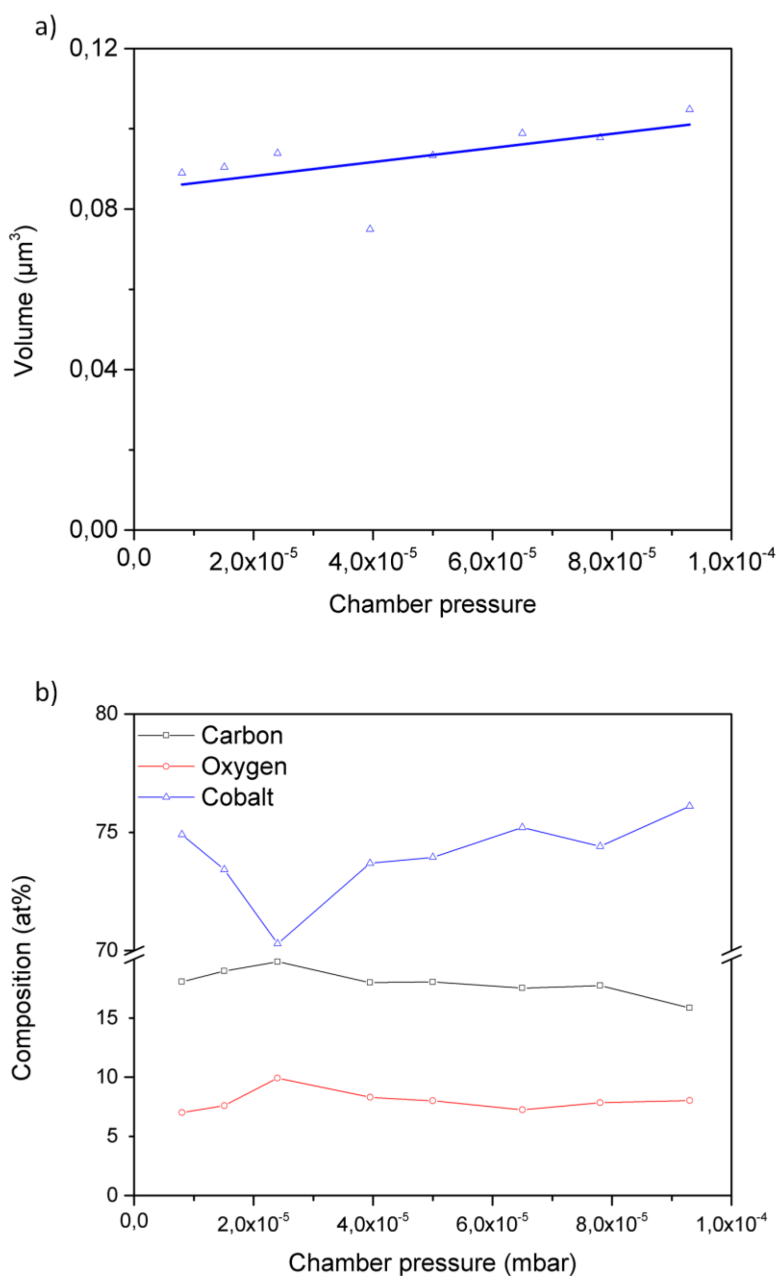

***Figure 33** - Deposited volume (a) and chemical composition trends (b) of the structures deposited at different fluxes of hydrogen. There was no significant change in volume due to the hydrogen flux. This is presumed to be because of the small size of the hydrogen atoms. Chemical composition was also largely unaffected.*

As **Figure 33** indicates, the effects of hydrogen on the growth rate of the deposits are very limited and seem to be below the estimated margin of error in volume measurement of +-0.02 μm^2. This can be explained by the very small size and mass of the hydrogen molecule when compared to a molecule of precursor. Due to this the

hydrogen atoms simply do not posses sufficient kinetic energy to give directionality to the precursor atoms in the reservoir. Chemical composition also is largely unaffected by the hydrogen carrier gas flux. Hydrogen is therefore nut suitable as a carrier gas for Co_2CO_8. While other precursors might benefit from deposition in the reducing hydrogen atmosphere, a benefit for deposition rate by physical kinetic energy transfer is also not expected in any case due to the small molecular mass of hydrogen.

4.3.3) Oxygen as a Carrier Gas

Also the injection of oxygen as a carrier gas was tested for stability of the chamber pressure. Stabilization of the chamber pressure took considerable longer compared to the other carrier gases, for medium values up to 25 minutes. Furthermore, the maximum flux of carrier gas corresponding to the limit value of the chamber pressure was again lower. A flux of 0.31 sccm resulted in a chamber pressure of 7.33×10^{-5} mbar and further increase would have stabilized above the limit of 1×10^{-4} mbar. **Figure 34** shows the correspondence between hydrogen flux versus chamber pressure.

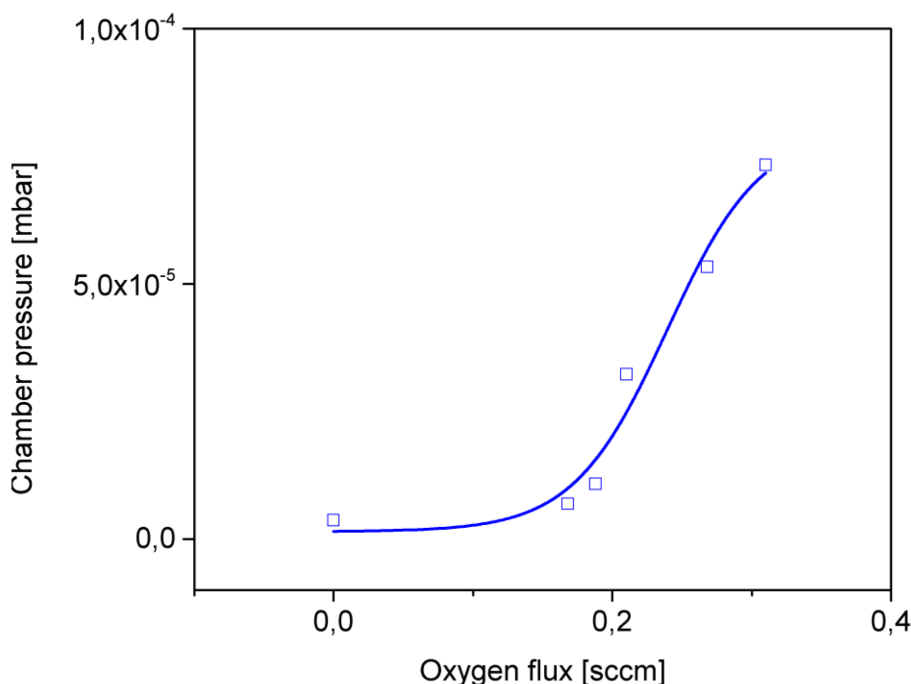

Figure 34 *- Influence of the flux of oxygen carrier gas on the pressure in the SEM chamber. Using oxygen as a carrier gas resulted in largely unstable chamber pressures. A flux change resulted in an intermittently stable chamber pressure after roughly 25 minutes that began to change again after several minutes. This behavior was observed at non-consistent but mostly intermediate values.*

Although the varying and increased time it takes for the pressure chamber to stabilize indicated some unknown processes happening, no adverse effects on either GIS or SEM were noticeable, so the experiments with oxygen were continued.

4.3.3a) Deposition Rate

Similar to hydrogen, oxygen was hoped to positively influence deposition chemistry by providing an oxidizing atmosphere. Using oxygen as a carrier gas, the stabilization of the chamber pressure proved much more difficult than with the other gases. At medium values the chamber pressure stabilized intermittently and started to rise again without any change in oxygen flux. Despite these problems, oxygen depositions were performed at all stable fluxes, the maximum of which was 0.318 sccm. Deposition rate as well as chemical composition was uncontrollable when

using oxygen as a carrier gas. Some, but non-consistent flux values showed greatly increased growth rate, but also suffered from a severe loss of geometry control (see **Figure 35**). At higher oxygen fluxes, deposition was dramatically reduced in most deposition series. As with the highly increased deposition rates, it was again not possible to systematically investigate this phenomenon due to the inconsistency of the results.

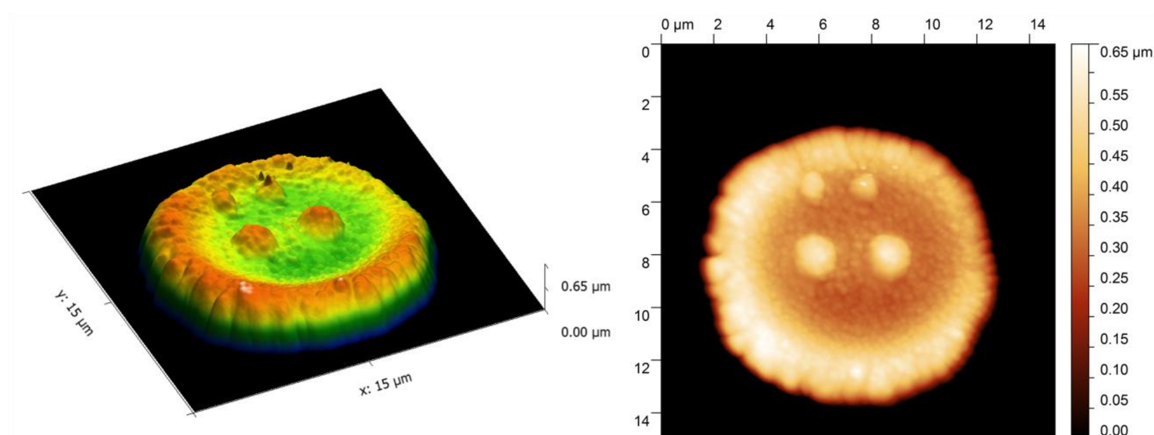

Figure 35 *– AFM 3D view and corresponding top-view of a structure deposited at a flux of 0.21 sccm demonstrating the loss of geometry control occurring usually at intermediate flux values of oxygen carrier gas. It is assumed that the precursor is dissociated and subsequently deposited prematurely inside the GIS line due to the oxygen atmosphere under which* Co_2CO_8 *is known to dissociate under release of CO.*

Due to the inability of consistent and geometrically true deposition, the idea of oxygen for the use as a carrier gas for Co_2CO_8 was discarded. It is assume that the precursor decomposes and gets partly deposited spontaneously inside the GIS line due to the presence of the oxygen atmosphere. Additionally, the precursor suffered severe color degradation inside the reservoir, requiring frequent cleaning and refilling of the precursor reservoir between deposition series.

5) Nanomagnet Logic (NML)

5.1) NML using three dimensional Fe structures by FEBID

5.1.1) Motivation

So far research in the area of NML has only been focused on the application of two dimensional magnetic structures. Part of this work, done in cooperation and under advisement of Dr. Gavagnin is on a new generation of NML structures using three dimensional structures.

Expanding the structures into the third dimension can be beneficial for NML in several ways. The first, most obvious way is a higher packing density, allowing for smaller footprints of the devices. This is because in addition to two dimensional nanowires, this new generation uses also three dimensional nanopillars. These nanopillars have a circular footprint of roughly 70 nm diameter as opposed to the nanowires footprint of roughly 40 x 400 nm^2. An additional possible benefit is the additional degree of freedom with regard to the magnetization axis. This will potentially ease the development of structures interfacing the magnetic devices with electrical architectures and clocking mechanisms.

The nanostructuring of magnetic as well as nonmagnetic material is usually done by classical lithographic methods. These methods, while absolutely established for parallel processing, take multiple process steps even for planar structures. Three dimensional structures are nearly impossible to quickly deposit using lithographic methods. Using FEBID, as a maskless, direct-write technique avoids these problems and therefore allows rapid development and prototyping of new NML designs.

5.1.2) Designs

Basic two dimensional design of NML structures has already been explained in chapter 2.1.2. In a second generation of NML the input and the so called helper magnets are fused together into a single, bent structure (see **Figure 36** (b)).

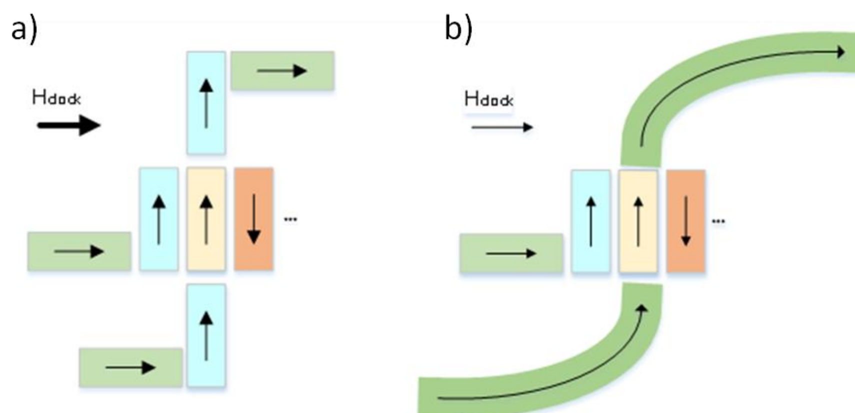

Figure 36 *– Schematic comparison of first (a) and second generation (b) NML majority gates. Two of the helper magnets (light blue) were fused with the input magnets to a single bent structure (green) in the second generation gates. This helped to reduce coupling errors significantly.*

Although, no systematic study on the reliability of the designs was performed, previous results by Dr. Gavagnin indicate that these second generation designs significantly decreased coupling errors. This comes as no surprise since there is one less gap for the magnetic field over which the magnetic field must couple into the next nanomagnet. The magnets however should remain in a single domain state to avoid unwanted or even unknown orientation of coupling areas of the nanomagnets. Therefore fusing of magnetic structures into a single one can only be performed if the resulting structure is not too large to remain in a single domain state.

Third generation NML combines the fusing of input and helper structures with using three dimensional nanopillars for all structures except the inputs. Several variations in the distances and heights of the nanostructures comprising the gate have been investigated. While there is clearly room for improvement the structure detailed in **Figure 37** represents the final state of this work. Since these pattern generator files do not really give a clear idea about the structure deposited, a more descriptive picture of this design in the form of an AFM 3D plot can be seen in chapter 5.2 (**Figure 41** (c)).

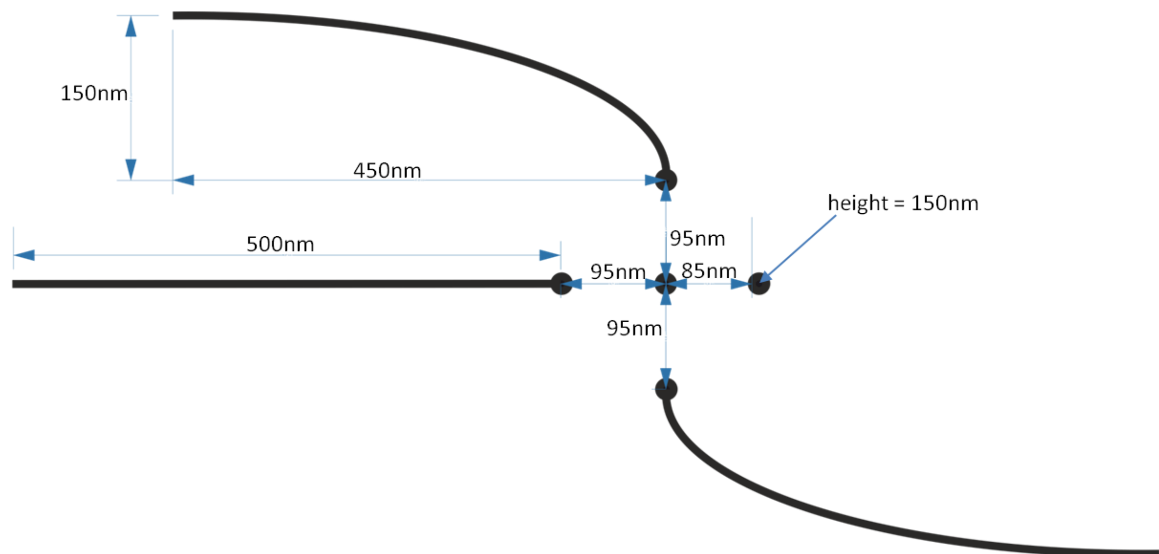

Figure 37 *– Final state of the research conducted in 3D NML majority gate designs in this work. The fused input / helper structures are combined with replacing helper and center magnets by three-dimensional nanopillars (line thickness and dot size are exaggerated compared to the pattern generator files for representation purposes).*

5.1.3) Experimental

NML structures were deposited from iron, using the precursor $FeCO_5$ at the mentioned standard conditions. The pressure in the Fe-GIS line was kept constant at 2.2 mbar using the needle valve. Chemical and structural analyses of these depositions have been investigated in [3,4].

After deposition the sample was magnetized in plane using an external electromagnet with a field strength of 1.8 kOe. This will set the inputs of the structures to a magnetization corresponding to 0 or 1 depending on the orientation of the input structure. Since so far there exists no viable I/O structure for directly manipulating the magnetic inputs, this external magnetic field resembles the clocking field that would in a finished device be created in situ. Subsequently the structures were examined by MFM as described in the previous chapter.

5.2) Results and Discussion

The first three dimensional design tested was a simple nanopillar made from iron and roughly 70 nm wide and 190 nm high. Due to the shape anisotropy these pillars are assumed to be in a single domain state. Before measurement these pillars are

magnetized externally by an electromagnet along their hard axis, *i.e.* in plane. After the removal of the external field the magnetization direction of the pillars should relax randomly into either upwards (out of the sample) or downwards (into the sample) since they are spaced far enough apart to avoid influencing each other. The results of the MFM measurement of a series of pillars are shown in **Figure 38**. The MFM phase image clearly shows that most of the pillars are magnetized in the same direction. This is most likely caused by an uncertainty in the angle of the pillar, as well as the direction of the external magnetic field. The shift of the contrast of the pillar center is assumed to be caused by a not perfectly perpendicular AFM tip.

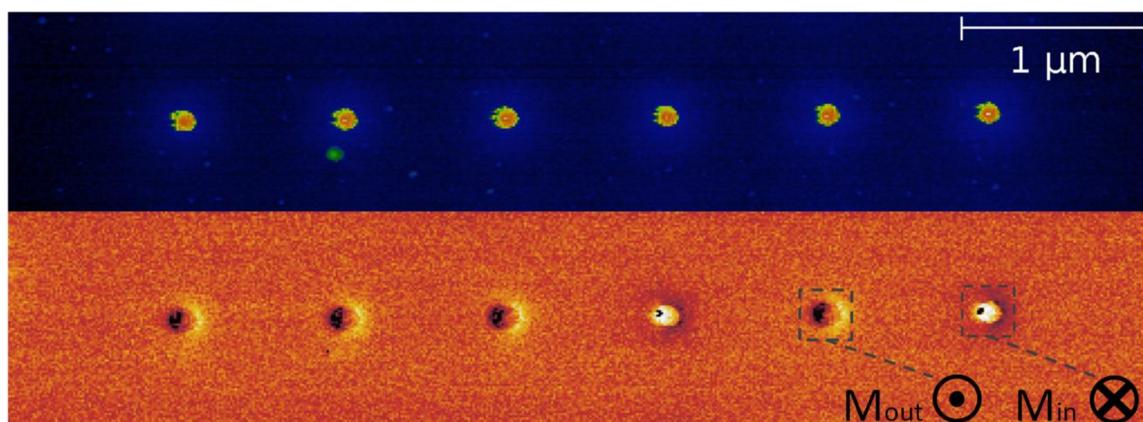

Figure 38 *–AFM (top) and corresponding MFM (bottom) of a row of iron nanopillars. They are deposited 1 µm apart to exclude magnetic coupling. Bright (dark) contrast again shows a magnetic field in an downward (upward) direction.*

The next investigation was concerned whether or not the magnetic coupling from a two dimensional nanowire to a perpendicular three dimensional nanopillar is working as expected. Therefore, a structure consisting of a horizontal nanowire in close proximity to a series of five identical nanopillars leading to another vertical nanowire has been investigated. After magnetizing in x-direction using the external electromagnet the horizontal nanowire is expected to influence the magnetization of the first nanopillar which in turn will transmit the information through the series of pillars and finally into the vertical nanowire. **Figure 39** shows an investigation and a schematic description of one of these test structures. As can be seen by the alternating contrast of the pillars and the consistent contrast of the nanowires the information is indeed transmitted from an in plane nanowire into out of plane

nanopillars and subsequently back to the in plane nanowire again. This can be seen as a proof of concept of the idea of bringing NML into the third dimension. While in the following AFM scans the pillars seem to be interconnected, it has been confirmed by SEM observation that they are in fact, separated. Due do the close proximity of the pillars (~30nm) the AFM tip is not able to pass between the pillars, interpreting them as a connected structure.

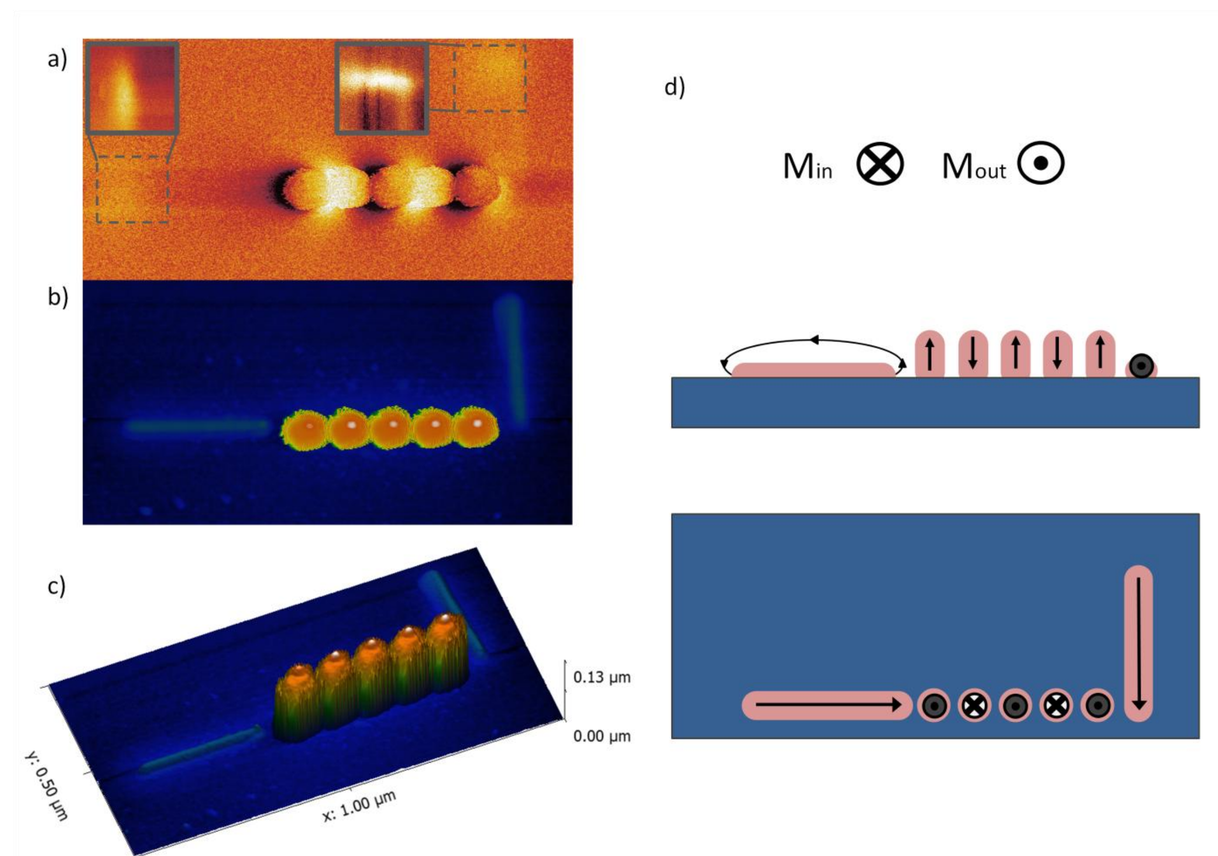

Figure 39 *– MFM (a), corresponding topographical (b) and 3D view (c) AFM investigations of a test structure. This structure was synthesized to test whether or not the information transfer between two dimensional nanowires and three dimensional nanopillars works as intended. (d) shows a schematic explanation of the magnetic field of the intended (and measured) magnetic orientations of the structures.*

After this proof of concept the first design of a majority gate was investigated. For this, all of the two dimensional nanowires except the input structures were replaced by three dimensional nanopillars. **Figure 40** shows an AFM / MFM analysis of the first three dimensional NML majority gate design. While this gate shows correct

alignment of the magnetic moments, more than half of the synthesized gates showed errors and did not display the correct contrast at the output.

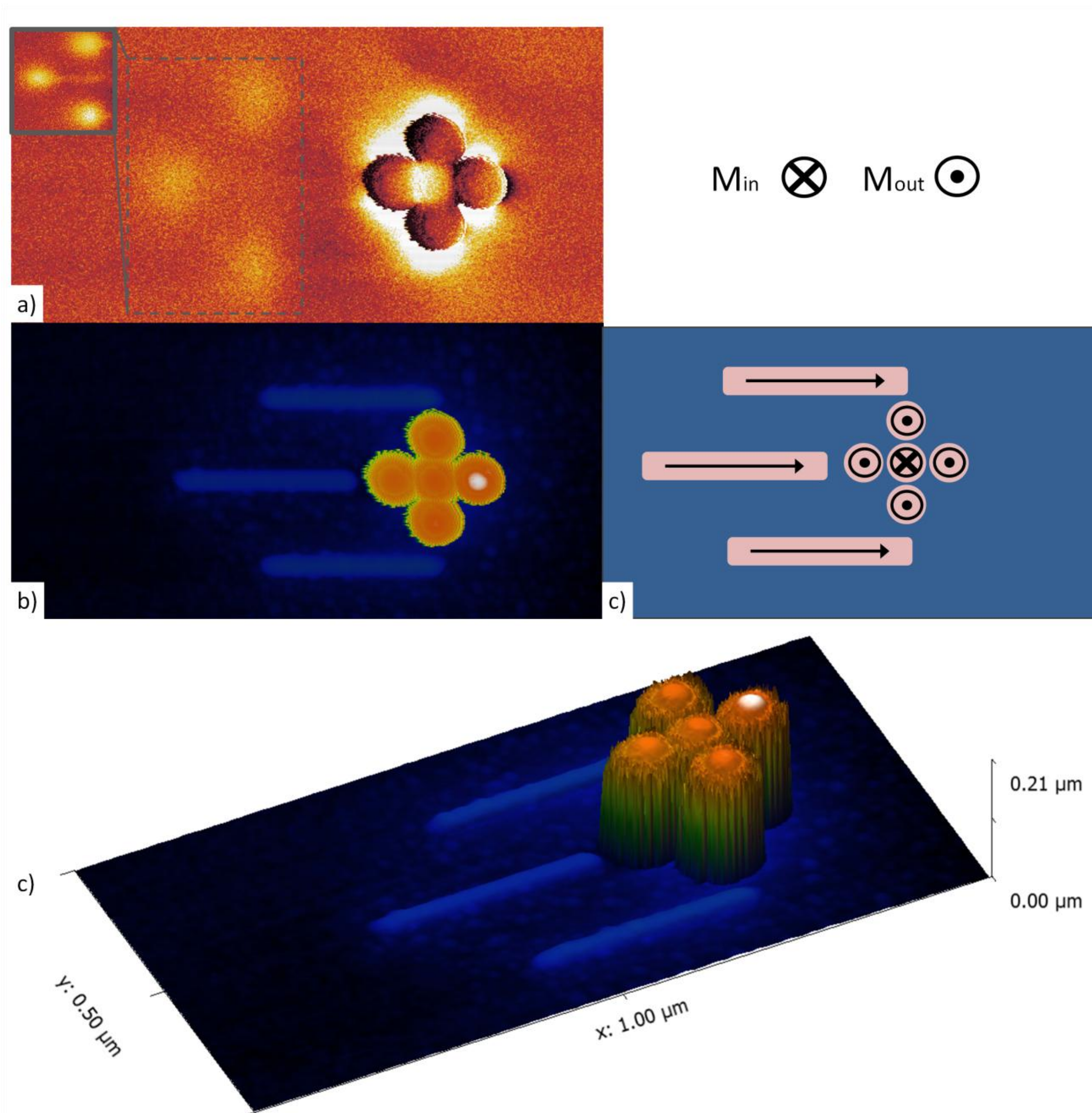

***Figure 40** – AFM investigations of the first generation 3D NML majority gate. (b) and (c) show the topographical and 3D AFM scans of the gate. (a) shows an MFM scan of the gate with the inset detailing the contrast of the input nanomagnets for better visibility. (c) shows a schematic representation of the magnetic configuration of the gate. The nanowire inputs couple ferromagnetically to the helper magnets (pillars) that influence the central pillar which in turn sets the magnetization of the output (rightmost) pillar.*

As with two dimensional NML, the next design step featured bent input nanowires on top of which the three dimensional nanopillar was deposited, again creating a fused structure of input and helper magnet. **Figure 41** shows an overview of several such

gates along with a close-up of one working gate. Using this design it was possible to achieve upwards of 65% correctly aligned majority gates.

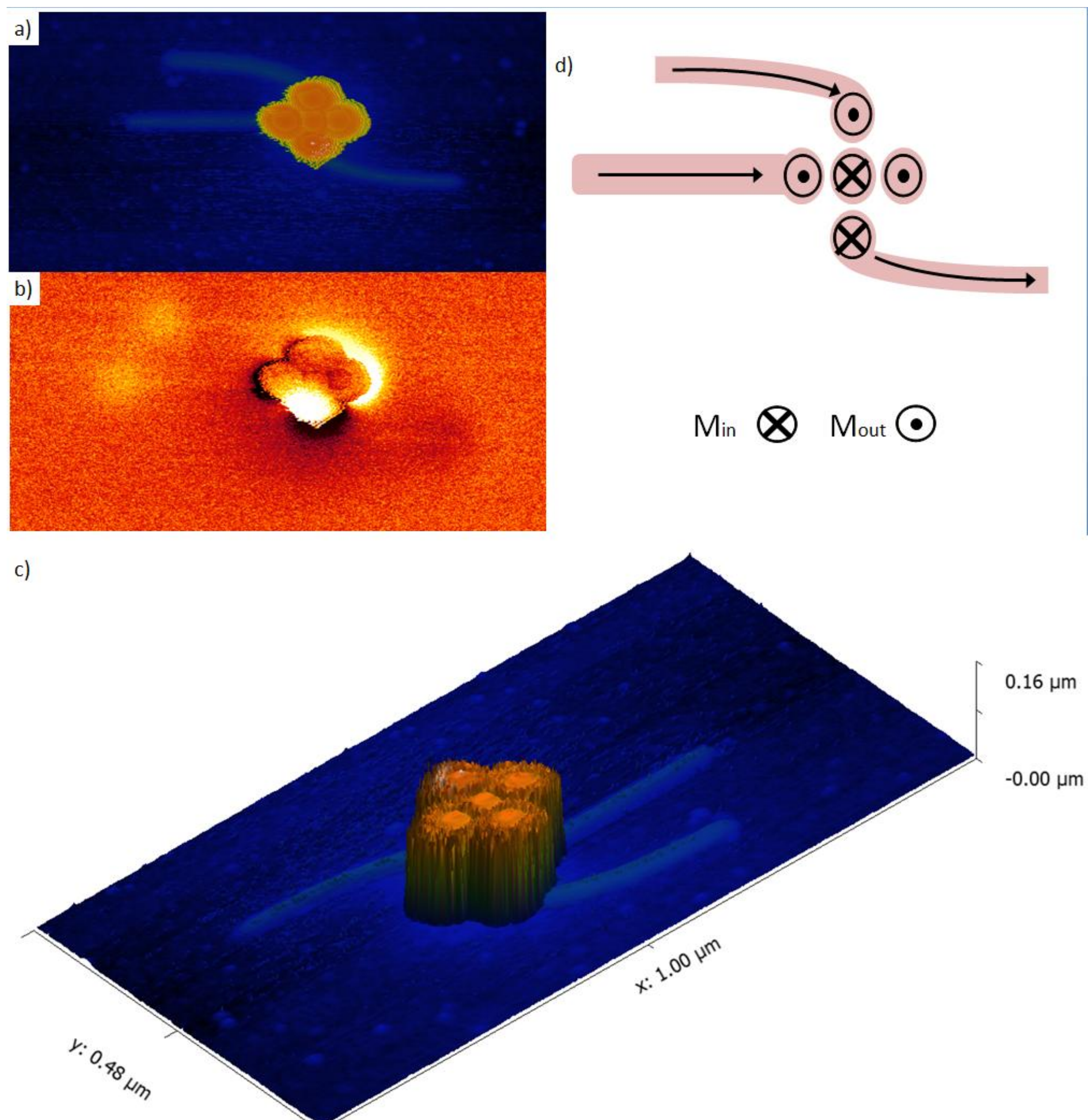

Figure 41 *– AFM investigation of the third generation majority gate. AFM (a) and MFM investigation (b) along with a 3D view from AFM and a schematic representation of the magnetic configuration (d) are shown. This combines the first generation three dimensional majority gate detailed in the previous figure and the fusing of input and helper structures to elliptical segments with nanopillars on top of them.*

While this design significantly improved the number of correctly aligned gates, one of the main problems during the investigations remained their sensibility to uncertainty

in the direction of the external magnetic field which due to the improvised nature of the sample holder in the electromagnet still exhibits a variation estimated at +-3 degrees.

6) Conclusion and Outlook

The main goal of this work was to find a way to reliable control the deposition of cobalt from the precursor Co_2CO_8 in order to enable further work on co-deposition of cobalt and iron. This is expected to be beneficial for NML because of cobalt's higher magnetic remanence field which is expected decrease coupling errors. A secondary goal was to develop further NML structures featuring three dimensional nanopillars.

For the first goal, a new type of GIS was built in cooperation with Dr. Gavagnin which enables the control of the precursor flux via the injection of a carrier gas. The carrier gas is controlled by an MFC and is keeping the atmosphere inside the precursor reservoir from saturating, thereby increasing the evaporation and subsequently the flux of precursor towards the chamber. Using inert nitrogen as a carrier gas, it was shown that accurate control of the precursor supply and subsequently the deposition regime is possible using this new GIS. Initial expectations that chemical reactions of the precursor with more reactive carrier gases, namely oxygen and hydrogen, could produce cleaner deposition were not verified in the case of Co_2CO_8. Hydrogen showed no discernible effect, neither on deposition rate nor chemical composition. Oxygen on the other hand resulted in uncontrolled deposition rates at several, but non-consistent flux values and a total loss of geometry control. Oxygen and hydrogen were therefore dismissed as a carrier gas for Co_2CO_8. Nitrogen as a carrier gas however showed excellent control of the deposition, thereby enabling further research into the co-deposition of cobalt and iron.

Simultaneously to the development of the co-deposition process, NML structures, were designed and deposited in iron using $FeCO_5$. The choice of this precursor was caused by the fact that it is can be injected without carrier gas at room temperature and is regularly deposited with our instrument. Therefore it was possible to focus the efforts on structure design instead of the optimization of deposition parameters. In this feasibility study, the joining of helper and input magnet was found to significantly reduce coupling errors. Further designs partly replacing the nanowires by three dimensional nanopillars were developed, adding an additional degree of freedom

with regards to the magnetic axis and increasing packing density due to the smaller footprint of the nanopillars compared to the nanowires.

Additional research is required to further optimize the gate structures and to devise an input / output scheme to interface the magnetic structures with electrical systems. Furthermore, additional carrier gases and precursors (or combinations thereof) should be investigated. While neither oxygen nor hydrogen seem to show the desired effects (at least not for Co_2CO_8), other reactive carrier gases like carbon-monoxide could lead to better deposition chemistry.

7) Appendices

7.1 List of Abbreviations

AFM	Atomic Force Microscope
BSE	Backscattered Electrons
CVD	Chemical Vapor Deposition
DT	Dwell Time
EDX	Energy Dispersive X-ray Spectroscopy
ELR	Electron Limited Regime
FEB	Focused Electron Beam
FEBID	Focused Electron Beam Induced Deposition
FEBIE	Focused Electron Beam Induced Etching
FSE	Forward Scattered Electrons
FWHM	Full Width Half Maximum
GIS	Gas Injection System
ITRS	International Technology Roadmap for Semiconductors
MFC	Mass Flow Controller
MFM	Magnetic Force Microscopy
NML	Nanomagnet Logic
PE	Primary Electrons
PLR	Precursor Limited Regime
PoP	Point Pitch (Step Size)
PTFE	Polytetrafluoroethylene (aka Teflon)

RF	Radio Frequency
RG	Residual Gas
RIE	Reactive Ion Etching
sccm	Standard Cubic Centimeter Per Minute
SE	Secondary Electrons
SEM	Scanning Electron Microscope
SL	Scan Loops (Exposure Loops)
TMHA	Tetramethylammonium
TMP	Turbomolecular Pump

7.2 List of Figures

Figure 1 *– Heat density trend of common consumer desktop CPUs. (taken from [8])* *13*

Figure 2 *– Magnetic stray field of different domain structures.* *14*

Figure 3 *– Shape anisotropy influence on the magnetostatic energy required for the magnetization of a body. (image from [16])* *15*

Figure 4 *– Magnetostatic energy in different orientation of the magnetization of a body.* *16*

Figure 5 *– Illustration of the nature of ferromagnetic or parallel (left) and anti-ferromagnetic or anti-parallel coupling (right)* *16*

Figure 6 *–Schematic design of a line or wire structure in NML.* *17*

Figure 7 *– Schematic design of a fanout structure used to spread binary signal to multiple sinks.* *18*

Figure 8 *– Schematic design of a majority gate in NML.* *19*

Figure 9 *– Illustration of the FEBID process.* *21*

Figure 10 *– CASINO simulation of the electron trajectories inside the substrate using a 3 kV electron beam* *23*

Figure 11 *– Schematic of a SEM column.* *24*

Figure 12 *– Schematic illustration of cause of the edge-effect* *25*

Figure 13 *- Lennard Jones (12,6) potential.* *28*

Figure 14 *– Schematic illustration of the optical pickup mechanism* *29*
Figure 15 – Schematic illustration of the different AFM modes. *29*

Figure 16 *– Schematic illustration of common AFM artifacts.* *31*

Figure 17 *– Schematic illustration of the MFM process.* *33*

Figure 18 *– Photograph of our SEM system used to perform FEBID.* *34*

Figure 19 *- Electron beam currents measured at all combinations of SEM apertures and acceleration voltages.* *35*

Figure 20 *– Schematic of the carrier gas enhanced GIS used in the experiments with* Co_2CO_8 .... *36*

Figure 21 *– Schematic of the second GIS used in the experiments with* $FeCO_5$ *38*

Figure 22 *– SEM micrograph of an overview of the samples alphanumeric pre-structuring* *41*

Figure 23 *– Schematic overview of the deposit designs used for the carrier gas investigations.* *42*

Figure 24 *– AFM micrograph of a square deposited for during the carrier gas investigations overlaid with the mask geometry used for the volume estimation of the deposits.* *46*

Figure 25 *–SEM micrograph of the FEBID tip used in the MFM investigations.* *47*

Figure 26 *– AFM (a) and corresponding MFM (b) investigation of a series of perpendicular iron nanowires. 48*

Figure 27 *– Influence of the flux of nitrogen carrier gas on the pressure in the SEM chamber ...51*

Figure 28 *– Geometrical investigations of the square structures. 53*

Figure 29 *– Deposited volume (a) and chemical composition trends (b) of the structures deposited at different fluxes of nitrogen. 55*

Figure 30 *– Deposited volume (a) and corresponding chemical composition trend (b) of the structures deposited at different beam currents. 57*

Figure 31 *– Full EDX spectrum of a structure deposited at 0.87 sccm. 58*

Figure 32 *– Influence of the flux of hydrogen carrier gas on the pressure in the SEM chamber..59*

Figure 33 *- Deposited volume (a) and chemical composition trends (b) of the structures deposited at different fluxes of hydrogen. 61*

Figure 34 *- Influence of the flux of hydrogen carrier gas on the pressure in the SEM chamber. .63*

Figure 35 *– AFM 3D view and corresponding top-view of a structure deposited at a flux of 0.21 sccm demonstrating the loss of geometry control 64*

Figure 36 *– Schematic comparison of first (a) and second generation (b) NML majority gates. ..66*

Figure 37 *– Final state of the research conducted in 3D NML majority gate designs in this work. 67*

Figure 38 *–AFM (top) and corresponding MFM (bottom) of a row of iron nanopillars. 68*

Figure 39 *– MFM (a), corresponding topographical (b) and 3D view (c) AFM investigations of a test structure. 69*

Figure 40 *– AFM investigations of the first generation 3D NML majority gate. 70*

Figure 41 *– AFM investigation of the third generation majority gate. 71*

7.3 Bibliography

[1] Niemier M., Bernstein G., Csaba G., Dingler A., Hu X., Kurtz S., Liu S., Nahas J., Porod W., Siddiq M., et al.,Nanomagnet logic: progress toward system-level integration, J Phys Condens Matter,2011,23,493202.

[2] Mart\in J., Nogues J., Liu K., Vicent J., Schuller I.K.,Ordered magnetic nanostructures: fabrication and properties, J Magn Magn Mater,2003,256,449–501.

[3] Gavagnin M., Wanzenboeck H.D., Belic D., Bertagnolli E.,Synthesis of Individually Tuned Nanomagnets for Nanomagnet Logic by Direct Write Focused Electron Beam Induced Deposition, ACS Nano,2012,7,777–84.

[4] Gavagnin M., Wanzenboeck H.D., Belic D., Shawrav M.M., Persson A., Gunnarsson K., Svedlindh P., Bertagnolli E.,Magnetic force microscopy study of shape engineered FEBID iron nanostructures, Phys Status Solidi A,2013.

[5] Córdoba R., Sesé J., De Teresa J., Ibarra M.R.,High-purity cobalt nanostructures grown by focused-electron-beam-induced deposition at low current, Microelectron Eng,2010,87,1550–3.

[6] Serrano-Ramón L., Córdoba R., Rodríguez L.A., Magén C., Snoeck E., Gatel C., Serrano I., Ibarra M.R., De Teresa J.M.,Ultrasmall functional ferromagnetic nanostructures grown by focused electron-beam-induced deposition, ACS Nano,2011,5,7781–7.

[7] Niemier M.T., Bernstein G.H., Csaba G., Dingler A., Hu X.S., Kurtz S., Liu S., Nahas J., Porod W., Siddiq M., et al.,Nanomagnet logic: progress toward system-level integration, J Phys Condens Matter,2011,23.

[8] Pop E.,Energy dissipation and transport in nanoscale devices, Nano Research,2010,3,147–69.

[9] Dingler A., Garrison M., Hu X.S., Niemier M., Alam M.T.,System-level energy and performance projections for nanomagnet-based logic. in Proc. 2009 IEEE/ACM Int. Symp. Nanoscale Architectures (NANOARCH), 2009, p. 21–6.

[10] Utke I., Hoffmann P., Melngailis J.,Gas-assisted focused electron beam and ion beam processing and fabrication, J Vac Sci Technol, B,2008,26,1197–276.

[11] Van Dorp W., Hagen C.,A critical literature review of focused electron beam induced deposition, J Appl Phys,2008,104,081301.

[12] Hoyle P., Ogasawara M., Cleaver J., Ahmed H.,Electrical resistance of electron beam induced deposits from tungsten hexacarbonyl, Appl Phys Lett ,1993,62,3043–5.

[13] Lundstrom M.,Applied physics. Moore’s law forever?, Science,2003,299,210–1.

[14] Vacca M., Graziano M., Zamboni M.,Nanomagnetic logic microprocessor: hierarchical power model, Very Large Scale Integration (VLSI) Systems, IEEE Transactions on,2013,21,1410–20.

[15] Morrish A.H.,The physical principles of magnetism, The Physical Principles of Magnetism, by Allan H Morrish, Pp 696 ISBN 0-7803-6029-X Wiley-VCH, January 2001,2001,1.

[16] Keplinger F.,Vorlesungsskriptum “Advanced Materials” TU Wien ,2011.

[17] Huth M., Porrati F., Schwalb C., Winhold M., Sachser R., Dukic M., Adams J., Fantner G.,Focused electron beam induced deposition: A perspective, Beilstein J Nanotechnol ,2012,3,597–619.

[18] Allwood D.A., Xiong G., Faulkner C., Atkinson D., Petit D., Cowburn R.,Magnetic domain-wall logic, Science,2005,309,1688–92.

[19] Chappert C., Fert A., Van Dau F.N.,The emergence of spin electronics in data storage, Nat Mat,2007,6,813–23.

[20] Stewart R.L.,Insulating films formed under electron and ion bombardment, Physical Review,1934,45,488.

[21] Christy R.W.,Formation of thin polymer films by electron bombardment, Journal of Applied Physics,1960,31,1680–3.

[22] Baker A.G., Morris W.C.,Deposition of metallic films by electron impact decomposition of organometallic vapors, Review of Scientific Instruments,1961,32,458–458.

[23] Amelinckx S., van Dyck D., van Landuyt J., van Tendeloo G.,Electron microscopy: principles and fundamentals. John Wiley & Sons; 2008.

[24] Prutton M., El Gomati M.M.,Scanning Auger electron microscopy. Wiley Online Library; 2006.

[25] 5 I.P.,Scanning Electron Microscopy ,2012, 18-29.

[26] Goldstein J.I., Newbury D.E., Echlin P., Joy D.C., Fiori C., Lifshin E., others,Scanning electron microscopy and X-ray microanalysis. A text for biologists, materials scientists, and geologists. Plenum Publishing Corporation; 1981.

[27] Binnig G., Quate C.F., Gerber C.,Atomic force microscope, Physical Review Letters,1986,56,930.

[28] Bhushan B.,Scanning probe microscopy in nanoscience and nanotechnology. Springer; 2010, 287-315.

[29] Giessibl F.J.,Advances in atomic force microscopy, Reviews of Modern Physics,2003,75,949.

[30] Müller D.J., Dufrene Y.F.,Atomic force microscopy as a multifunctional molecular toolbox in nanobiotechnology, Nature Nanotechnology,2008,3,261–9.

[31] Mühl T., Körner J., Philippi S., Reiche C., Leonhardt A., Büchner B.,Magnetic force microscopy sensors providing in-plane and perpendicular sensitivity, Applied Physics Letters,2012,101,112401.

[32] Häberle T., Haering F., Pfeifer H., Han L., Kuerbanjiang B., Wiedwald U., Herr U., Koslowski B.,Towards quantitative magnetic force microscopy: theory and experiment, New Journal of Physics,2012,14,043044.

[33] Vock S., Wolny F., Mühl T., Kaltofen R., Schultz L., Büchner B., Hassel C., Lindner J., Neu V.,Monopolelike probes for quantitative magnetic force microscopy: Calibration and application, Applied Physics Letters,2010,97,252505.

[34] Kuramochi H., Asada H., Uzumaki T., Yui H., Iitake M., Takano F., Akinaga H., Manago T.,Material dependence of magnetic force microscopy performance using carbon nanotube probes: Experiments and simulation, Journal of Applied Physics,2014,115,093907.

[35] Wolny F., Mühl T., Weissker U., Lipert K., Schumann J., Leonhardt A., Büchner B.,Iron filled carbon nanotubes as novel monopole-like sensors for quantitative magnetic force microscopy, Nanotechnology,2010,21,435501.

[36] Friedli V., Utke I.,Optimized molecule supply from nozzle-based gas injection systems for focused electron-and ion-beam induced deposition and etching: simulation and experiment, J Phys D: Appl Phys ,2009,42,125305.

[37] Wachter S., Gavagnin M., Wanzenboeck H.D., Shawrav M.M., Beli’c D., Bertagnolli E.,Nitrogen as a carrier gas for regime control in focused electron beam induced deposition, Nanofabrication,2014,1.

[38] Utke I., Bret T., Laub D., Buffat P., Scandella L., Hoffmann P.,Thermal effects during focused electron beam induced deposition of nanocomposite magnetic-cobalt-containing tips, Microelectron Eng,2004,73,553–8.

[39] Lau Y., Chee P., Thong J., Ng V.,Properties and applications of cobalt-based material produced by electron-beam-induced deposition, J Vac Sci Technol, A,2002,20,1295–302.

[40] Fowlkes J.D., Randolph S.J., Rack P.D.,Growth and simulation of high-aspect ratio nanopillars by primary and secondary electron-induced deposition, J Vac Sci Technol, B,2005,23,2825–32.

[41] Córdoba R., Fernández-Pacheco R., Fernández-Pacheco A., Gloter A., Magén C., Stéphan O., Ibarra M.R., De Teresa J.M.,Nanoscale chemical and structural

study of Co-based FEBID structures by STEM-EELS and HRTEM, Nanoscale Res Lett,2011,6,1–6.

[42] Su M.-S., Tsai K.-Y., Lu Y.-C., Kuo Y.-H., Pei T.-H., Yen J.-Y.,Architecture for next-generation massively parallel maskless lithography system (MPML2). SPIE Advanced Lithography, 2010, p. 76371Q–76371Q.